

MASTER'S THESIS

POST-PROCESSING TECHNIQUES FOR OPTICAL COHERENCE  
TOMOGRAPHY: COMPUTATIONAL ABERRATION CORRECTION IN  
PHASE UNSTABLE SYSTEMS AND COMPLEX NOISE REDUCTION

Sebastián Ruiz Lopera  
[sruizlo2@eafit.edu.co](mailto:sruizlo2@eafit.edu.co)

Universidad EAFIT  
School of Sciences  
Master in Applied Physics  
Applied Optics Group  
Medellín  
2020



POST-PROCESSING TECHNIQUES FOR OPTICAL COHERENCE  
TOMOGRAPHY: COMPUTATIONAL ABERRATION CORRECTION IN  
PHASE UNSTABLE SYSTEMS AND COMPLEX NOISE REDUCTION

SEBASTIÁN RUIZ LOPERA

Thesis submitted in partial fulfillment of the requirement for the degree of  
Master in Applied Physics

Supervisors

Ph.D. RENÉ RESTREPO GÓMEZ  
Área de Instrumentación óptica espacial  
Intituto Nacional de Técnica Aeroespacial

Ph.D. NÉSTOR URIBE PATARROYO  
Wellman center for photomedicine  
Harvard Medical Shcool and Massachussets General Hospital

UNIVERSIDAD EAFIT  
SCHOOL OF SCIENCES  
MASTER IN APPLIED PHYSICS  
APPLIED OPTICS GROUP  
MEDELLÍN  
2020



ACCEPTANCE NOTE

---

---

Supervisor

---

---

Examiner

---

---

Examiner

---

---

Medellín, September 2020



*“A grad student in procrastination tends to stay in procrastination unless an external force is applied to it.”*

**Newton’s first law of Graduation**



---

# CONTENTS

<b>LIST OF FIGURES</b>	<b>IX</b>
<b>LIST OF TABLES</b>	<b>XI</b>
<b>LIST OF ACRONYMS</b>	<b>XIII</b>
<b>1 Introduction</b>	<b>15</b>
1.1 Optical coherence tomography . . . . .	15
1.2 Aberrations in OCT . . . . .	18
1.3 Noise in OCT . . . . .	19
1.4 Problem statement . . . . .	21
1.5 Objectives . . . . .	22
1.5.1 General objective . . . . .	22
1.5.2 Specific objectives . . . . .	22
1.6 Outline of the work . . . . .	23
1.7 Structure of the document . . . . .	24
<b>2 Theoretical basis</b>	<b>26</b>
2.1 Optical coherence tomography . . . . .	26
2.1.1 Measuring the echo time delay of light . . . . .	27
2.1.2 Low coherence interferometry . . . . .	27
2.1.3 Time domain OCT . . . . .	30
2.1.4 Fourier domain OCT . . . . .	32
2.1.5 Optical frequency domain imaging . . . . .	34
2.1.6 Phase stability in OCT configurations . . . . .	36
2.2 Modelling the acquisition of the complex OCT signal . . . . .	40

2.2.1	Confocal gating for lateral scan in OCT . . . . .	41
2.2.2	Forward model . . . . .	42
2.3	Refocusing and computational aberration correction techniques in OCT	45
2.3.1	Interferometric synthetic aperture microscopy . . . . .	47
2.3.2	Digital refocusing . . . . .	48
2.3.3	Computational adaptive optics . . . . .	50
2.3.4	Phase stability requirement . . . . .	54
<b>3</b>	<b>Computational aberration correction in phase unstable OCT: SHARP</b>	<b>61</b>
3.1	SHARP: A CAO technique for OCT . . . . .	61
3.1.1	Phase stability assessment . . . . .	61
3.1.2	Description of the method . . . . .	61
3.2	Proof of concept experimental validation . . . . .	61
3.3	Extending SHARP . . . . .	61
3.3.1	Motion artifacts correction . . . . .	61
3.3.2	Spatially-varying aberrations correction . . . . .	61
3.3.3	Complex amplitude noise reduction . . . . .	61
<b>4</b>	<b>Complex shot noise reduction in OCT: CTNode</b>	<b>62</b>
<b>5</b>	<b>Experimental application</b>	<b>63</b>
<b>6</b>	<b>Conclusions and future works</b>	<b>64</b>
<b>REFERENCES</b>		<b>65</b>



---

# LIST OF FIGURES

1.1	Example of axial scan and cross-section images generated by OCT measuring the magnitude and echo time delay of backscattered light.	16
1.2	Schematic of a generic OCT setup based on a Michelson interferometer and illustration of common notation used for axial axis, transverse axes (fast/slow scan axes), axial scan (A-line) and cross-sectional images (B-scan, en face).	18
2.1	Schematic of generic Michelson interferometer used in OCT.	28
2.2	Schematic of a generic TDOCT setup based on a Michelson interferometer, where axial scan is performed by displacing the reference mirror in the axial axis while recording the interference with a mono-pixel detector.	31
2.3	Illustration of A-lines obtained in OCT. a) Axial reflectivity profile for a sample characterized by three reflectors: b) TDOCT A-line, c) spectral interferogram and d) FDOCT A-line obtained as the Fourier transform of c), indicating the background (DC), cross-correlation (c.c.) and auto-correlation (a.c.) components.	31
2.4	Schematic of a generic SDOCT setup based on a Michelson interferometer, where axial scan is obtained by computing the Fourier transform of the spectral interferogram acquired with a digital spectrometer.	34
2.5	Schematic of a fiber-based SSOCT setup where the wavelength-swept source changes its instantaneous central wavelength in time due to the rotation of the polygonal mirror. A trigger signal to start the acquisition of the spectral interferogram is produced by the fiber Bragg grating that is designed to reflect a single wavelength, indicating the start of a sweep cycle of the light source.	37

2.6 Schematic of generic a) LF-SDOCT setup for acquisition of a B-scan in a single detector shot and b) FF-SSOCT setup for acquisition of a tomogram in a single cycle of the wavelength-swept source. Red path illustrates the illumination beam and blue path the image formation on detector plane for a point. . . . .	40
2.7 Illustration of confocal gating for light with $\lambda_c = 1\mu\text{m}$ . a) Focused beam produced by two optical systems with relatively low and high NA. b) Relation between confocal parameter and transverse resolution. . . . .	42
2.8 Simulation of an OCT image in high-NA regime. a) Sample consisting of randomly located point scatterers, b) Gaussian beam of the system with NA= 0.25 and c) OCT image simulated using the forward model, displayed in logarithmic scale. . . . .	45
2.9 Simulation of an OCT image in low-NA regime. a) Sample consisting of randomly located point scatterers, b) Gaussian beam of the system with NA=0.1 and c) OCT image simulated using the forward model, displayed in logarithmic scale. . . . .	46
2.10 Illustration of digital refocusing. a) Sample consisting of randomly located point scatterers, b) OCT image simulated using the forward model, c) Digital refocused. b) and c) are displayed in logarithmic scale. . . . .	50
2.11 Illustration of computational adaptive optics. Simulated OCT en face image a) without and b) with aberrations and defocus, induced using the wavefront in e). Result of c) digital refocusing and d) computational adaptive optics. a)-d) are displayed in logarithm scale. . . . .	55
2.12 Illustration of Shannon's entropy metric to measure image sharpness of a defocused en face image corrected using Zernike polynomial $Z_4$ . Plot shows the value of SE as a function of correction weight $\tilde{\alpha}_4$ . Surrounding en faces images were corrected with different weights for a visual inspection of image quality. Optimal corrected image (on the red rectangle) corresponds to the minimum value of SE. . . . .	56
2.13 Illustration of the impact of motion in digital refocusing. a) OCT image simulated using the forward model, a) with static sample; b) with sample motion shown in d), that results in the unsuccessful digital refocused image c) refocusing. Note the relative shift between A-lines when comparing the insets in red rectangles. . . . .	58

---

## LIST OF TABLES

---

# LIST OF ACRONYMS

**APDL** *ANSYS parametric design language* (Lenguaje paramétrico de diseño de ANSYS).



# CHAPTER 1

---

## INTRODUCTION

Light-matter interaction have become an important tool in medical sciences and biology, leading to the creation and development of a specialized field known as *biomedical optics* or *biophotonics* oriented to fundamental research, imaging, diagnosis, therapy and monitory of diseases and surgery assistance []. Many imaging techniques have emerged to cover the general necessity to visualize internal structures of tissues, in particular, *Optical Coherence Tomography* (OCT) has become an important imaging modality for biomedical optics and medicine []. A general introduction to the operation and applications of OCT in medicine is given in the following sections.

### 1.1. Optical coherence tomography

OCT is an imaging technique that produces three-dimensional, micrometric-resolution images of scattering samples such as biological tissues by measuring the light that is backscattered by the sample using low-coherence interferometry [].

Research community in biophotonics have showed great interest in OCT given its unique features such as high sensitive that allows to obtain useful information from biological samples with different optical properties, and its resolution of 1-15  $\mu\text{m}$  and axial range of  $\sim 2$  mm that fills a gap between other medical imaging modalities such as ultrasound and confocal microscopy []. Furthermore, non-invasive operation of OCT, both ex vivo and in vivo, with not contrast agents nor ionizing radiation are important features that have positioned OCT in the medical community for imaging of tissue pathologies *in situ* and in real time, particularly in ophthalmology [], but also in intravascular imaging [], endoscopic imaging [] and dermatology [].

OCT produces cross-sectional and volumetric images by measuring the magnitude and “echo time delay” of light backscattered by the sample [], similarly to the operation of other tomography techniques, such as ultrasound that employs sound instead of light. Backscattered light contains information of the optical properties of the sample and information at different depths can be distinguished by determin-

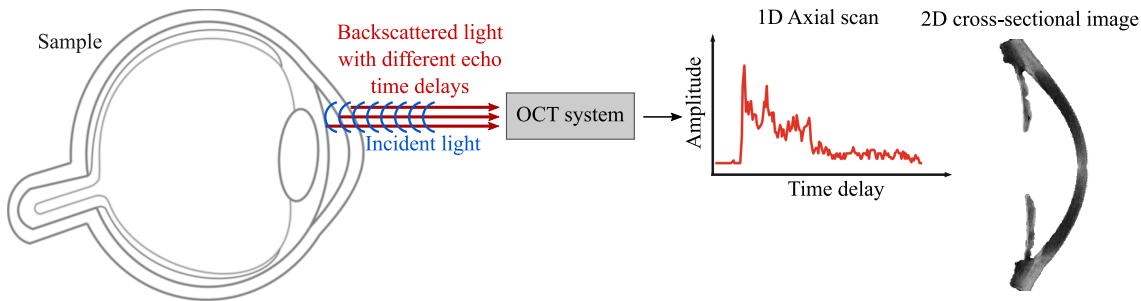


Figure 1.1: Example of axial scan and cross-section images generated by OCT measuring the magnitude and echo time delay of backscattered light.

ing the time it takes for light to travel different axial distances, thus performing an axial scan that can be expanded to a cross-sectional image as depicted in Figure 1.1 and also to volumetric images. Given the large magnitude of speed of light of  $\sim 3 \times 10^8 \text{ m/s}$ , there are technical limitations to make electronic devices with the required sensitivity and time resolution to measure the echo time delay of light with micrometric resolution [6]. Hence, OCT employs low-coherence interferometry to measure the backscattered light in terms of optical path length differences rather than measuring directly the temporal delays [6], being both related through the speed of light.

Providing cross-sectional images *in situ* and in real time without the need to remove and process specimens is an important feature of OCT for the visualization of tissue micro-structure and pathology. This possibility to perform “optical biopsies” enables operation of OCT in application where histopathology of excised tissue, the gold standard for assessing pathology, is insufficient for various reasons [6]; (1) biopsy is hazardous or impossible, for example in the eye, arteries or nervous tissues, (2) biopsy is susceptible to sampling errors, given the impossibility to precisely detect the location of the pathology, for example in cancer diagnosis, leading to false negative, (3) real time visualization is required, for instance in guidance of invasive procedures, and (4) structural information is not sufficient and additional functional imaging or measurements like blood flowmetry is necessary.

Several phenomena occur in the interaction of the sample and the incident light. OCT measures only the light that is backscattered, in other words, the light that is scattered in the opposite direction of the incident beam. In that sense, major limitation of OCT is that light is highly scattered in multiple directions by most tissues reducing the portion of backscattered light, and this attenuation by scattering imposes a limit to imaging depth in OCT to  $\sim 2 \text{ mm}$  in tissue [6]. Light sources in the near-infrared range with wavelength between 840–1300 nm are widely used for OCT given the low water absorption and high scattering of tissue. In general, imaging at  $\sim 1300 \text{ nm}$  is preferred in most OCT applications because it provides

larger imaging penetration compared to shorter wavelengths [], although standard for ophthalmology are  $\sim 850$  nm and  $\sim 1 \mu\text{m}$  wavelengths [].

OCT has become an important standard for clinical assessment in ophthalmology given that the optical transparency of the eye allow “easy” optical access to the retina, and in general to the posterior segment of the eye. Actually, first experimental demonstration of optical coherence tomography imaging in 1991 by Huang et al. was performed in human retina and coronary artery ex vivo [], then following works by Fercher et. al [] and Swanson et al. [] demonstrated retinal images in vivo, and since then, ophthalmology has been the specialty with more clinical studies and technical developments in OCT, because it assists in the diagnosis of diseases in early and late stages, even before visual symptoms or irreversible consequences occur, and it also allows to track progression of diseases and monitor response to therapy.

The most direct application of OCT after ophthalmology is in dermatology given the easy access to skin tissue. OCT allows readily identification of skin features like sweat ducts, dermal/epidermal junction and collagen-rich structures, but imaging depth is very limited due to the highly scattering properties of skin tissue. Although it is an active application for OCT, medical impact of OCT in dermatology is not as relevant as in ophthalmology given that practical and scientific benefits over standard medical procedures in this field are not clear.

Medical applicability of OCT was extended with the integration of OCT imaging systems with catheters, endoscopes and needles probes that enable operation of OCT in luminal tissue such as gastrointestinal tract, vasculature and airway, as well as in solid organs. The possibility to image internal body organs *in situ* is particularly important when excision of tissue is not possible or hazardous, for instance in intravascular imaging, which has became a relevant medical OCT application.

Moving to an experimental description of OCT, the general setup consists in a light source, an optical interferometer such as Michelson or Mach-Zender interferometers, and a light detector, as depicted in Figure 1.2. In the interferometer, light from the light source is divided into two beams, one is reflected by a mirror, the other by the sample, and both are recombined producing interference that is captured by the detector. The axis in which light propagates is referred as *axial* axis and the orthogonal axes are known as *lateral* or *transverse* axes. Most OCT systems focus the light into a small spot in the sample and acquire the axial scan known as *A-line*, relating the amplitude of the signal versus depth. Then, the position of the focused spot in the transverse plane is changed using two galvanometer mirrors and in each position an A-line is acquired, this is known as raster scan. Acquisition of A-lines at different positions of the sample along one lateral axis known as *fast scan axis* produces 2D cross-sectional views known as *B-scans*. Acquisition of B-scans

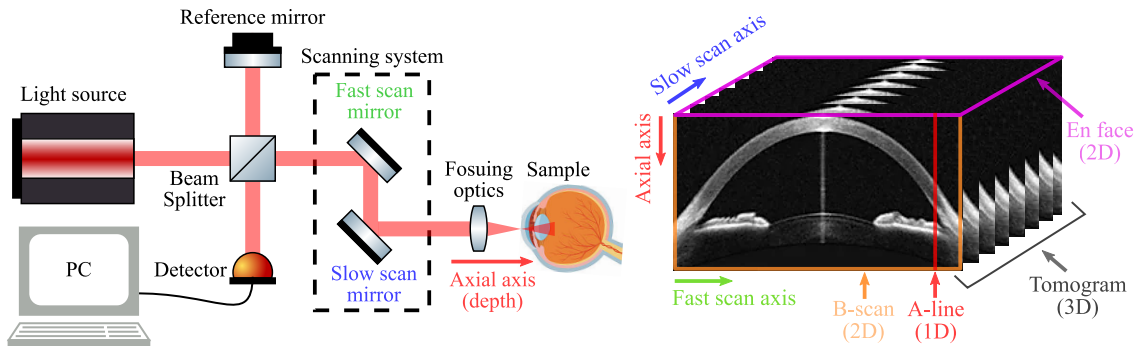


Figure 1.2: Schematic of a generic OCT setup based on a Michelson interferometer and illustration of common notation used for axial axis, transverse axes (fast/slow scan axes), axial scan (A-line) and cross-sectional images (B-scan, en face).

at different positions of the sample along the lateral axis that is orthogonal to the fast scan axis, known as *slow scan axis*, provides volumetric images or *tomograms*. Furthermore, cross-sectional views relating the two lateral axes at a fixed depth are known as *en face*. See Fig. 1.2 for an illustration of the notation described above.

From this general scheme, OCT technology and theory have evolved and to date there is a wide variety of system configurations with particular advantages in terms of imaging speed, sensitivity, imaging depth, among others. Nonetheless, the use of an optical system to focus the light into the sample and to collect the backscattered light is common to any OCT system and its properties greatly influence the quality of images, most notably, it determines the lateral resolution, i.e. the resolution in the lateral axes, and it may induce optical aberrations that degrade image quality, similarly to any other optical imaging technique.

## 1.2. Aberrations in OCT

In most OCT systems, light is focused into the sample, so that lateral resolution is defined by the diffraction limit spot size of the focused light beam [1]. Optical aberrations, whether from the optical systems or the sample itself, degrade image quality affecting the visualization of fine structures and limiting the axial range where images appear sharp [2]. To avoid or reduce impact of aberrations, specialized optical systems are used, for instance, telecentric and achromatic systems correct for spherical and chromatic aberrations.

One of the greatest limitations of optical systems is that in-focus images are only obtained for those planes of the sample that are within the *depth of field* (DoF), defined by the numerical aperture (NA) of the system, while beam divergence causes a resolution loss for planes outside the DoF, producing defocused images. In the case

of OCT, this means that certain planes of the tomogram will be in-focus and appear sharp, but others are out-of-focus and appear blurred. To avoid this, systems with large DoF of  $\sim 0.5 - 2$  mm are commonly used so that imaging axial range is limited by signal attenuation in tissue rather than by the effect of defocus. However, this is achieved at the cost of reducing lateral resolution given its inverse relation with DoF, well-known as lateral-resolution–DoF trade-off. By this reason, it is very common that resolution in the transverse plane is lower than resolution in the axial axis, which depends on the central wavelength and spectral bandwidth of the light source and is independent of the NA [1]. In addition to system-induced aberrations, the sample can introduce aberrations with a significant impact to reduce image quality, particularly in ophthalmology given that light beam passes through the eye and the cornea and the lens may induce aberrations [2].

High-resolution imaging is a very active research field in OCT since it gives access to additional and more detailed information of the sample, which is important in many applications, for example, in cellular imaging as eye photoreceptors [3]. To obtain high-resolution images, aberration can be corrected with hardware-based adaptive optics (AO) [4] or computational aberration correction (CAC) [5]. In AO, additional hardware is used to correct for wavefront distortions *in situ*. It demands complex optics and system design that limits clinical applicability, yet, it is incapable of compensating the lateral-resolution–DoF trade-off given that each depth demands an individual correction but OA applies a global correction.

CAC operates the complex OCT signal using mathematical models based on the propagation of light to compensate aberrations using an appropriate phase filter. CAC addresses lateral-resolution–DoF trade-off and its major limitation is the reduction of signal strength given that acquired signal is weaker in the presence of aberrations, which is an experimental limitation that, in principle, cannot be corrected in post-processing. Currently, operation of CAC is not possible in all OCT systems due to technical limitations that prevent the acquisition of reliable complex-value tomograms.

In this work, we present a method for CAC suitable for most common OCT systems to expand its applicability throughout research and clinical applications, making it possible to correct for optical aberration to improve image quality by post-processing in systems where it was not possible due to technical limitations.

### 1.3. Noise in OCT

Any contribution to the measured signal apart from the backscattered light, that is the interest of OCT, can be considered as *noise*. In that sense, *speckle* arising in tissue imaging as a consequence of coherent interference of backscattered light

with random phases, is not noise in rigorous terms, indeed, speckle is important for several functional applications [], but in practical terms it causes random fluctuations that hinder visual interpretation. Consequently, speckle reduction while preserving visibility of fine structures is an active area of research in OCT [] and in most coherent imaging techniques, such as synthetic aperture radar (SAR) [].

Noise reduction in OCT is generally associated with speckle reduction, but there are multiple sources of strictly speaking noise in the OCT signal induced by the system, that have a relevant impact on imaging features such as the *signal-to-noise-ratio* (SNR), define as the ratio of the signal power and the noise process variance [], the sensitivity, defined as the SNR of a perfect reflector placed in the sample arm, and the dynamic range, defined as the range of SNR observable within a signal acquisition or image []. SNR is typically given in decibels (dB) thought the logarithmic transformation  $\text{SNR}_{\text{dB}} = 10 \log_{10} \text{SNR}$ . Developments in OCT technology had a significant improvement in sensitivity and current imaging systems achieve sensitivities as high as  $\sim 100$  dB, meaning that minimum detectable reflectivity in the sample is  $\sim 1 \times 10^{-10}$  times the reflectivity of an ideal reference mirror. In experimental terms, OCT images span dynamic ranges of 40–60 dB although it depends on the application.

Most notable sources of noise in the OCT signal are shot, excess and thermal noise. *Shot* noise originates from the uncertainty of “counting” particles of discrete nature such photons and electrons, and it arises in the detection of the OCT signal that involves photon-electron conversion and digitization. *Excess* noise arises from time fluctuations of the incident intensity, mostly due to fluctuation of the emission of the light source. *Thermal* noise stems from random motion of electrons in conductors. In OCT, noise has been addressed mostly experimentally, and at this points it is possible to achieved shot noise limited detection []. For instance, excess noise suppression is achieved using two detectors in a *balanced* detection scheme where non-interfering light that contributes the most to excess noise is suppressed. Computational approaches for noise reduction have concentrated in speckle suppression, and most shot noise reduction approaches rely on straightforward average of multiple frame repetitions [].

Reduction of signal strength due to aberrations have a negative impact in SNR and dynamic range because the collected signal is intrinsically lower in the presence of aberrations than the aberration-free case, and this is not compensated in CAC techniques. An experimental approach to reduce signal strength loss is to use CAC techniques in systems with an astigmatic beam that provides high signal strength throughout longer depth than a Gaussian beam, so that aberrations are corrected including astigmatism induced on purpose.

## 1.4. Problem statement

Post-processing is important in OCT to obtain images with high resolution and contrast as well as additional useful information of the sample, improving and facilitating study, diagnosis and monitory of diseases, and CAC is a clear example of the potential of the complex OCT signal for post-processing. Developing techniques to improve image quality in OCT has been the scope of collaborative projects between the Applied Optics Group at Universidad EAFIT and the Wellman Center for Photomedicine at Massachusetts General Hospital and Harvard Medical School. Results include the development of an useful technique for reduction of *speckle* [], that in general is considered as noise that hinders image visualization, as well as the derivation of models for robust estimation of the autocorrelation function of intensity OCT signal [] that is the basis of functional imaging modalities such as angiography [] and flowmetry []. In parallel, experimental setups have been made, including a lab-made accessible full field OCT system [] and a linear-in-wavenumber spectrometer for spectral-domain OCT []. In addition, a numerical phase correction algorithm was proposed but, given its iterative structure, processing times are unpractical [] and results are limited, however, this initial approach for phase stabilization contributed to ideas and notions that led to the proposal of this work.

Computational aberration correction is a very active field in OCT to improve image quality in application where aberration have a significant impact [] and to provide high-resolution images []. Development of CAC techniques has been constrained to the development of OCT systems configurations that allow a more reliable and robust measurement of the complex-valued tomogram. CAC techniques are based on a common mathematical model, so that, requirements for its application are the same, being phase stability the most relevant requirement. *Phase stability* is achieved when there is a constant phase relation between measurements at different lateral locations, in other words, when there exists a correlation between measurements.

Acquisition of phase stable tomograms is not straightforward in practical terms given that phase is very sensitive to phase noise that affects phase stability, arising from the imaging system and from the sample itself due to axial motion. In fact, sample motion artifacts include two effects, the first is a phase jump due to Doppler effect [] and the second is the effective shift of the complex information due to sample displacement. Doppler phase noise is the issue mostly addressed for CAC given that its impact is in general more notable than impact of complex-amplitude shift, although the impact of each effect is relative to features of the imaging system and the amount of motion.

Achieving sufficient phase stability for CAC has restricted its usage to custom system configurations with volumetric phase stability, that in some cases is achieved

at the cost of increasing system complexity. In phase stable systems, operation of CAO is straightforward and for in vivo imaging it is sufficient to correct for phase noise due to sample axial motion using numerical corrections based on reference phase signal, generated by adding a highly reflective surface such as a coverslip, or based on the acquired sample signal. Drawback of correction methods based on reference phase signal is that it demands hardware modifications to add a highly reflective surface in addition to the reference mirror.

Numerical phase correction methods based on the sample signal assume that there is phase stability at least along one lateral axis, thus correction is only required along the orthogonal lateral axis. This assumption is valid for phase stable systems in which phase instabilities in the tomogram arise from sample motion and only affect one lateral axis, commonly the slow scan axis. However, there are common OCT configurations that present phase noise induced in the system, for which current numerical phase corrections are hopeless given that there is not any axis with phase stability. Operation of CAO in such phase unstable configurations rely on hardware modifications to avoid system-induced phase noise, restricting its applicability in research and medical application.

Given the current limitation of standard OCT systems to acquire phase stable tomograms, the proposal of this work is *to develop and experimentally test a post-processing method for optical aberration correction in phase unstable tomograms, with not need for hardware modifications or specialized configurations, hence enabling operation of CAC for image quality improvement in system unsuitable for it so far, namely, raster scan wavelength-swept source OCT systems.*

In addition, we also aim to address other important issues in CAC, in regard to the SNR reduction in aberrated tomograms due to signal strength loss, as well as the motion artifacts affecting the complex amplitude, not only the phase.

## 1.5. Objectives

### 1.5.1. General objective

To correct optical aberrations in optical coherence tomography with phase unstable systems using post-processing.

### 1.5.2. Specific objectives

- To establish the state-of-art of computational aberration correction in optical coherence tomography.
- To identify sources of phase noise and phase correction methods for optical

coherence tomography.

- To develop a computational method for phase stabilization and aberration correction of tomograms with not intrinsic phase stability.
- To test the performance of the method with ex vivo and in vivo tomograms acquired with typical phase unstable OCT systems.
- To identify and analize the possible limitation of the method.

## 1.6. Outline of the work

In this work we present our technique Short Aline-Range Phase-stability adaptive-optics (SHARP) for computational aberration correction in phase unstable systems, showing successful experimental results in different OCT applications using systems with no need for specific hardware that ensure phase stability. SHARP integrates a computational aberration correction technique with numerical phase noise correction to compensate aberrations in phase unstable OCT tomograms, showing particular potential for extending the depth-of-field.

Furthermore, approaches to address other general drawbacks and limitations of CAC are proposed. On the one hand, complex noise reduction approaches are presented to countervail the intrinsic reduction of SNR in computational aberration corrected images when compared to experimental aberration-free images. Second, SHARP is extended to admit tomograms affected by complex amplitude shifts due to sample motion for in vivo imaging, in addition to Doppler phase term, thus addressing both effects of motion artifacts.

There is a particular interest in this work in noise reduction because of its importance not only in CAC but in OCT imaging universally to improve sensitivity and dynamic range. First proposal for noise reduction is to use a straightforward frequency filter grounded in the context of image deconvolution, that has been used in several imaging modalities, for instance in astronomy, but not in the context of OCT, to the best of our knowledge. In fact, this filter is useful for image deconvolution but is not particularly dedicated to noise reduction.

Second approach is a more effective noise reduction technique that we developed and termed Coherent Tomographic Non-local-means denoising (CTNode). This technique is an adaptation of our previous despeckling technique Tomographic Non-local-means despeckling (TNode) where modifications were made in order to address for photon noise in the complex amplitude tomogram, that is the aim of CTNode, instead of speckle in the intensity tomogram, that is the aim of TNode. Both approaches are based on non-local-means weighted-averaging using statistical

properties of its corresponding undesired component, i.e. photon noise or speckle. Experimental results of CTNode are presented in conjunction to SHARP, although applicability of both techniques is independent.

## 1.7. Structure of the document

In this Chapter, a general introduction of OCT was provided to present the problem and the objectives of this work.

In Chapter 2, there is a description of the principle of operation of OCT and the different possible configurations. A model for the signal of the “OCT experiment” is presented from a interferometric perspective and then from a light propagating and image formation perspective. The latter model serves as the basis for the CAC techniques that are then explained, followed by a description of the level of phase stability that is experimentally obtained and the current phase-noise correction methods, emphasising in numerical approaches. A simulated tomogram with simple structures generated elsewhere based on the acquisition of the complex OCT signal [] is used to illustrate concepts and explanations when required.

Foundation and description of SHARP are given in detail in Chapter 3. Results of a proof-of-concept experiment are presented, in which a cucumber sample presenting remarkable structures was used to acquire tomograms with and without defocus induced intentionally shifting the position of the sample. Furthermore, approaches to address additional important issues in CAC, beside phase stability requirement, are proposed, namely, motion artifacts and spatially-varying aberration correction.

Mathematical and conceptual framework of CTNode is presented in Chapter 4. First, a simple model for the origin and description of photon noise in the OCT signal is explained, as well as the statistical description of complex noise. Then, TNode is summarized and finally the presented models for photon noise are used to formulate CTNode in detail. Results of a proof-of-concept experiment are presented, in which we added synthetic noise to the simulated noiseless tomogram mentioned in Chapter 2 and then filtered with CTNode, being the original noiseless tomogram a “ground-truth” to assess performance of CTNode.

Experimental validation of the methods is presented in Chapter ?? for a variety of samples, systems and applications, including ex vivo and in vivo imaging in ophthalmic and endoscopic OCT. Aberration correction with SHARP is demonstrated in anterior segment imaging of swine eye ex vivo, endoscopic OCT of swine airway in vivo, and skin imaging of human hand dorsal in vivo with motion artifacts. Furthermore, it is showed that integration of SHARP and resolution-preserving despeckling technique TNode dramatically improves image quality in comparison to the raw

tomograms. Also, noise reduction with CTNode is demonstrated in conjunction with SHARP and independent, showing a significant noise floor reduction. Then, a discussion and analysis of the methods and the results is given, highlighting the capabilities and drawbacks.

Finally, conclusions in regard to results and objectives of the work are discussed in Chapter 6, as well as possible further steps in the context of computational aberration correction in OCT.

# CHAPTER 2

---

## THEORETICAL BASIS

There have been several theoretical and technical advances in optical coherence tomography (OCT) in response to the importance that it has gathered in the biomedical optics community. In this chapter, principle of operation, models for the OCT signal and advances of OCT are explained, including the different configurations that have been developed, starting from the initial approach based on low coherence interferometry in time domain detection that later advanced into spectral domain detection, and presenting advantages and disadvantages in practical features such as sensitivity, imaging speed, and most importantly here, phase stability that is discussed in detail. In the first part of this Chapter, Section 2.1, the OCT experiment is analyzed from an interferometric perspective in regard to the coherence gating used for axial scan performed in OCT. In second part, Section 2.2, propagation of light in the sample arm is taken into account to establish a model for image formation in OCT, in regard to the confocal gating used for transverse scan. From this model derive the state-of-the-art techniques for computational aberration correction in OCT explained in Section 2.3, where also phase stability requirement and approaches to achieve it are discussed.

### 2.1. Optical coherence tomography

*Tomography* techniques produce images by sectioning the sample using a penetrating wave [1]. In medicine, tomography techniques radiate waves into the sample and measure the backscattered waves to produce cross-sectional images of the internal structure of tissues. For instance, ultrasound employs sound waves and measures the echo time delay and amplitude of the reflected waves [2], while light is used in optical coherence tomography [3]. Measuring the echo time delay of light with micrometric resolution using direct electronic detection schemes as in ultrasound is challenging given that light is around six orders of magnitude faster than sound. Therefore, optical ranging measurements demand alternative approaches such as high-speed optical gating or low coherence interferometry that is the basis of OCT.

### 2.1.1. Measuring the echo time delay of light

Using backscattered light to see through biological tissue was proposed by Duguay [] in 1971 employing a high-speed optical Kerr shutter with a 10 pico-seconds pulsed laser to “photograph light in flight” while propagating through a cell of milk and water []. In subsequent approaches, resolution was improved using nonlinear optical processes to detect the time delay of backscattered light with femto-second resolution, making possible to measure corneal thickness in a rabbit eye *ex vivo* with  $15 \mu\text{m}$  resolution []. Drawbacks of these approaches are the use of intense pulsed lasers and that sensitivity is as low as  $-70$  dB while current OCT systems achieve sensitivities of  $-100$  dB, three order of magnitude greater.

### 2.1.2. Low coherence interferometry

Potential of low coherence interferometry to measure echo time delay of backscattered light with high resolution and sensitivity was devised in the 80s decade, starting with optical fibers and waveguide devices [] and later with biological samples after the first demonstration by Fercher et al. in 1986 [] measuring the axial eye length. Interferometry techniques measures the correlation between optical fields by interfering light that is backscattered by the sample with light that has traveled through a reference path. In a interferometer, light emitted by the source is splitted into two arms, one is reflected by a reference mirror and the other is reflected by the sample, and then both are recombined to produce interference in a detection plane. Interference only occurs when the optical path length (OPL) difference between the two light beams is within the *coherence length* of the light source  $l_c$ . This is the optical distance that different waves from the same light source can mismatch and yet maintain a *degree of coherence* or a *correlation*.

Coherence of a light source is determined by its emission spectrum: coherence length is larger for narrower emission spectrum. The key insight in low coherence interferometry is that the use of low coherence light reduces the coherence length, hence *interference signal at a given OPL can be distinguished from interference signals at others OPL with a resolution equal to the coherence length*. This *coherence gating* establishes the principle of axial scan in OCT. For a Gaussian spectrum with central wavelength  $\lambda_c$  and full-width at half-maximum  $\Delta\lambda$ , axial resolution  $\delta z$  is

$$\delta z = \frac{2 \ln 2}{\pi} \frac{\lambda_c^2}{\Delta\lambda}. \quad (2.1)$$

Inverse relation between  $\delta z$  and  $\Delta\lambda$  shows that light source with broad emission spectrum provides high axial resolution. To derive the axial OCT signal, consider

the Michelson interferometer depicted in Figure 2.1.

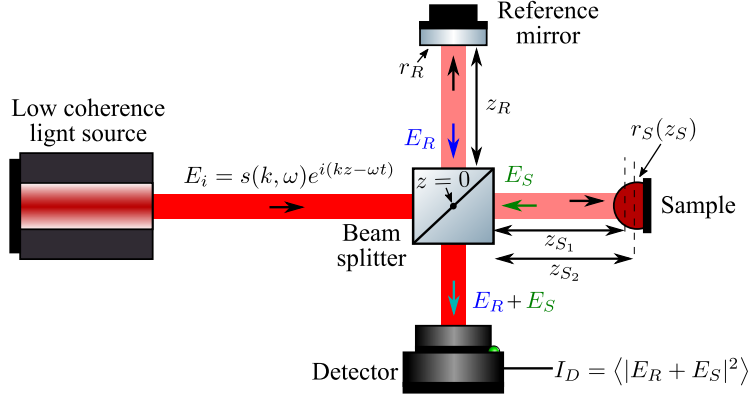


Figure 2.1: Schematic of generic Michelson interferometer used in OCT.

Interferometry measures the correlation between the electric fields of the light reflected by the sample and the reference mirror. Consider that the light source emits plane waves with electric field  $E_i = s(k, \omega)e^{i(kz - \omega t)}$  at time  $t$  and distance  $z$  along the propagation axis, being  $s(k, \omega)$  the complex amplitude, dependent on the angular frequency  $\omega$  and wavenumber  $k = 2\pi/\lambda$  for wavelength  $\lambda$ . Assuming free space propagation and a 50/50 beam splitter, the reference beam propagates a distance  $z_R$  from the beam splitter to the reference mirror with reflectivity  $r_R$  and reflectance  $R_R = |r_R|^2$ , then reflected light propagates back to the beam splitter and its electric field can be expressed as  $E_R = \frac{E_i}{\sqrt{2}} r_R e^{i2kz_R}$ .

On the other hand, light on the sample arm propagates a distance  $z_S$  from the beam splitter to the sample. In biological tissues, the refractive index changes resulting in different reflectivities [], therefore, the sample can be described as a discrete number  $N$  of reflectors with reflectivities  $r_{S_n}$  and reflectances  $R_{S_n} = |r_{S_n}|^2$  located at distances  $z_{S_n}$  as

$$r_S(z_{S_n}) = \sum_{n=1}^N r_{S_n} \delta(z_S - z_{S_n}). \quad (2.2)$$

**Coherent gating in OCT allows to reconstruct the function  $\sqrt{R_{S_n}(z_{S_n})}$  to produce images with optical contrast related to changes in the refractive index of the sample.**

Light backscattered by the sample propagates back to the beam splitter with electric field  $E_S = \frac{E_i}{\sqrt{2}} \sum_{n=1}^N r_{S_n} e^{i2kz_{S_n}}$ . Reference and sample electric fields  $E_R$  and  $E_S$  interfere and a photodetector with responsivity  $\rho$  captures the intensity producing

a photocurrent  $I_D(k, \omega)$  that can be described as

$$\begin{aligned} I_D(k, \omega) &= \rho \left\langle \left| \frac{E_R}{\sqrt{2}} + \frac{E_S}{\sqrt{2}} \right|^2 \right\rangle \\ &= \rho \left\langle \left| \frac{E_i}{2} r_R e^{i2kz_R} + \frac{E_i}{2} \sum_{n=1}^N r_{S_n} e^{i2kz_{S_n}} \right|^2 \right\rangle \\ &= \frac{\rho}{4} \left\langle \left| s(k, \omega) r_R e^{i2kz_R - \omega t} + s(k, \omega) \sum_{n=1}^N r_{S_n} e^{i2kz_{S_n} - \omega t} \right|^2 \right\rangle, \end{aligned} \quad (2.3)$$

assuming  $z = 0$  at the splitting surface of the beam splitter without loss of generalization, where  $\langle \cdot \rangle$  is the temporal averaging performed by the photodetector during the integration time of a single measurement, that is long enough to expect that  $I_D$  is independent of the temporal component  $\omega t$  given the fast temporal oscillation of light imposed by  $\omega$ . This is consequent with expansion of Eq. (2.3) using  $|E|^2 = E^* E$  that yields the spectral interferogram

$$\begin{aligned} I_D(k) &= \frac{\rho}{4} \left[ S(k) \left( R_R + \sum_{n=1}^N R_{S_n} \right) \right] \dots \\ &\quad + \frac{\rho}{2} \left[ S(k) \sum_{n=1}^N \sqrt{R_R R_{S_n}} \cos(2k [z_R - z_{S_n}]) \right] \dots \\ &\quad + \frac{\rho}{4} \left[ S(k) \sum_{n \neq m}^N \sqrt{R_{S_n} R_{S_m}} \cos(2k [z_{S_n} - z_{S_m}]) \right]. \end{aligned} \quad (2.4)$$

where  $S(k) = |s(k, \omega)|^2$  is the light source spectrum and  $z_R - z_{S_n}$  is the OPL difference.

There are three components in  $I_D(k)$  as noted in Eq. (2.4). First one is a *background* component that is independent of propagating distances and it is the largest component given that typically reference mirror reflectivity denominates the sample reflectivity. In general, this is an undesired component that is canceled out using background removal methods [].

Second is a *cross-correlation* component that depends on the spectrum of the light source  $S(k)$ , the wavenumber  $k$  and the OPL difference  $z_R - z_{S_n}$ . This is the desired component in OCT imaging since it gives access to the sample reflectivity through the term  $\sqrt{R_R R_{S_n}}$ .

Last term is an *auto-correlation* component that represents the interference between the different sample reflectors, independent of the reference light. This is

commonly an artifact component that can be neglected increasing the magnitude of the other two components by increasing the reference mirror reflectivity.

Note that  $I_D(k)$  in Eq. (2.4) is the interference resulting from a particular wavenumber  $k$ , but the ultimate aim in OCT is to “isolate” the  $\sqrt{R_R R_{S_n}}$  term along depth, that is related to OPL differences  $z_R - z_{S_n}$ . There are two approaches to retrieve the depth-dependent photocurrent  $i_D(z)$ , yielding two major OCT configurations: time domain OCT (TDOCT) and Fourier domain OCT (FDOCT). Also, note that depth-dependent signal  $i_D(z)$  is given for a specific transverse point with coordinates  $(x, y)$  of the sample. In raster scan systems, the beam is scanned in the sample plane using galvanometer scan mirror that deflects the light beam, and in each position  $(x, y)$  an A-line is acquired. Given that the interest here so far is the axial scan, dependence on coordinates  $(x, y)$  is omitted for simplicity.

### 2.1.3. Time domain OCT

Most straightforward way to obtain the depth-dependent signal is to use a mono-pixel detector to capture the interference while the reference delay  $z_R$  is scanned by moving the reference mirror along the axial direction as shown in Figure 2.2. The detector captures the intensity for all  $k$  at the same time, thus  $i_D(z_R)$  is the integration over all  $k$  of  $I_D(k)$ ,

$$i_D(z_R) = \frac{\rho}{4} S_0 \left( R_R + \sum_{n=1}^N R_{S_n} \right) \dots + \frac{\rho}{2} S_0 \sum_{n=1}^N \sqrt{R_R R_{S_n}} e^{-(z_R - z_{S_n})^2 \Delta k^2} \cos [2k_0 (z_R - z_{S_n})]. \quad (2.5)$$

where  $S_0 = \int_0^\infty S(k) dk$  is the spectral total power emitted by the light source, and a normalized Gaussian spectrum  $S(k) = \frac{1}{\Delta k \sqrt{\pi}} e^{-\left[\frac{(k-k_0)}{\Delta k}\right]^2}$  is assumed, being  $k_0$  the central wavenumber and  $\Delta k$  the full-width at  $1/e$  of the maximum.

Time domain A-line  $i_D(z_R)$  consists of a background component (DC), proportional to  $S_0$ , and an interference component that is a summation of Gaussian functions with finite width, having peak-values of  $\sqrt{R_R R_{S_n}}$  located at OPL differences  $z_R - z_{S_n}$  and modulated by cosines of period  $\pi/k_0$ , equivalent to  $\lambda_0/2$ .  $\gamma(z_R) = e^{-(z_R - z_{S_n}) \Delta k^2}$  is known as the *coherence function* and it causes a “broaning” of the interference signal of each reflector and its width is related to the coherence length of the light source that determines the axial resolution, thus  $\gamma(z_R)$  is considered as the axial point-spread function (PSF). Figure 2.3 illustrates a TDOCT A-line

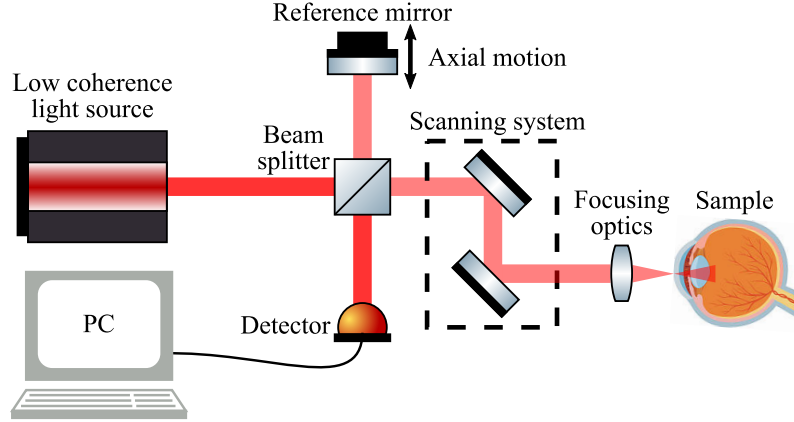


Figure 2.2: Schematic of a generic TDOCT setup based on a Michelson interferometer, where axial scan is performed by displacing the reference mirror in the axial axis while recording the interference with a mono-pixel detector.

in Fig.2.3(b) for a sample characterized by three reflectors as shown in Fig.2.3(a).

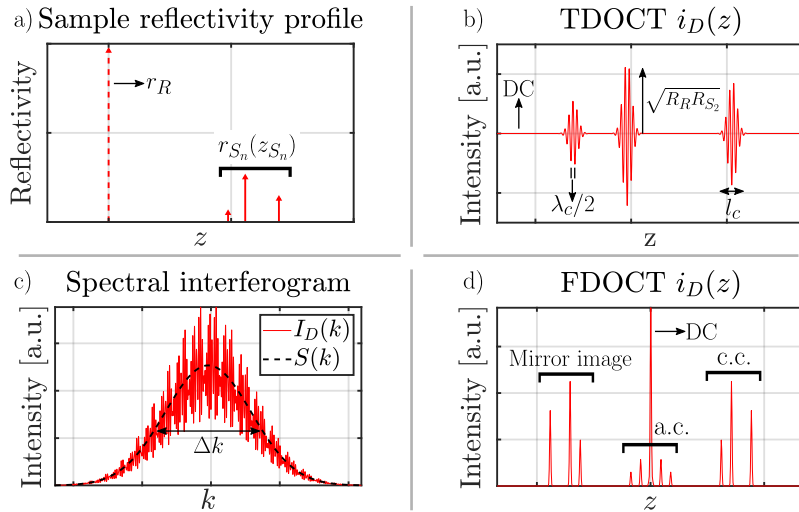


Figure 2.3: Illustration of A-lines obtained in OCT. a) Axial reflectivity profile for a sample characterized by three reflectors: b) TDOCT A-line, c) spectral interferogram and d) FDOCT A-line obtained as the Fourier transform of c), indicating the background (DC), cross-correlation (c.c.) and auto-correlation (a.c.) components.

Early OCT imaging systems including the first experimental demonstration of OCT in 1991 [] employed a time domain detection. Designation of time domain arises from the fact that the reflectivity axial profile of the sample is acquired while displacing the reference mirror in time. This demands mechanical systems to displace the reference mirror and this limits imaging speed to A-line rates  $<\sim 2$  kHz, due to technical restrictions to develop precise fast motion systems with micrometric resolution and millimetric travel range. Furthermore, given that axial scan is acquired while the detector captures the signal at different times, stable systems are

required to avoid artifacts during imaging due to changes of the imaging system, for instance, changes of the light source emission. By this reason, achievable sensitivity is limited, and this in addition to low imaging speed establish the major drawbacks of TDOCT.

#### 2.1.4. Fourier domain OCT

Although TDOCT systems served well in early medical OCT development, their relatively slow scan rate and limited sensitivity restricted the potential of OCT and restricted its expansion to many medical applications. An improvement in sensitivity and imaging speed in OCT was possible with the introduction of FDOCT systems where the reference mirror remains fixed. Spatial and optical frequency domains are conjugate domains with the wavenumber and the OPL being Fourier transform duals. This concept led to development of Fourier domain acquisition where photocurrent  $I_D(k)$  in Eq. (2.4) is captured directly in the  $k$  space and a subsequent Fourier transform  $\text{FT}_k \{\cdot\}$  of the signal along variable  $k$  yields the depth-dependent photocurrent  $i_D(z)$ , with not need to displace the reference mirror.

Using the Fourier transform property  $\text{FT}_k \{\cos(kz_0)\} = \frac{1}{2} [\delta(z + z_0) + \delta(z - z_0)]$ , the convolution theorem  $\text{FT}_k \{g(k)f(k)\} = \text{FT}_k \{g(k)\} * \text{FT}_k \{f(k)\}$ , and the shifting property of delta functions  $f(z) * \delta(z - z_0) = f(z_0)$ , it is possible to obtain the FDOCT A-line  $i_D(z) = \text{FT}_k \{I_D(k)\}$  from Eq. 2.4 as

$$\begin{aligned} i_D(z) &= \frac{\rho}{8} \gamma(z) \left[ R_R + \sum_{n=1}^N R_{S_n} \right] \dots \\ &+ \frac{\rho}{4} \sum_{n=1}^N \sqrt{R_R R_{S_n}} [\gamma(2[z_R - z_{S_n}]) + \gamma(-2[z_R - z_{S_n}])] \dots \\ &+ \frac{\rho}{8} \sum_{n \neq m=1}^N \sqrt{R_{S_n} R_{S_m}} [\gamma(2[z_{S_n} - z_{S_m}]) + \gamma(-2[z_{S_n} - z_{S_m}])], \end{aligned} \quad (2.6)$$

where again  $\gamma(z) = \text{FT}_k \{S(k)\}$  is the coherence function of the source, that assuming a Gaussian emission spectrum is given by

$$S(k) = \frac{1}{\Delta k \sqrt{\pi}} e^{-\left[\frac{(k-k_0)}{\Delta k}\right]^2} \xleftrightarrow{\text{FT}} \gamma(z) = e^{-z^2 \Delta k^2}. \quad (2.7)$$

Eq. (2.6) contains three components as Eq. (2.4); background, cross-correlation and auto-correlation components. Figure 2.3 shows an example of a Fourier domain A-line in Fig. 2.3d) for a sample with three reflectors as shown in Fig. 2.3a) and its corresponding interferogram in  $k$  space in Fig. 2.3c). Cross-correlation component

provides access to the signal of interest in OCT  $\sqrt{R_R R_{S_n}}$  by each reflector appearing at positions  $\pm 2(z_R - z_{S_n})$  and being “broadened” by the coherence function similarly to the case of the TDOCT A-line. The apparent position of the reflectors  $\pm 2(z_R - z_{S_n})$  have a factor of 2 since the interferometer measures the round-trip distance.

There is a “mirror image” produced by the fact that  $I_D(k)$  is real, hence its Fourier transform is Hermitian symmetric, that is, the positive values are the complex conjugate of the negative values, and this is represented in the double sign of  $\pm 2(z_R - z_{S_n})$ . This does not have an important influence if the sample is positioned entirely in one side of the zero OPL, such that it is possible to extract only one half of the Fourier spectrum to avoid the mirror image.

Background component appears as a large component centered at the zero OPL. In general, it can be easily omitted from the signal since the reflectors of the sample are positioned beyond the zero OPL such that cross-correlation terms do not overlap with the background component. However, additional to the main lobe, side lobes may appear and cause significant artifacts overlapping with the cross-correlation terms, therefore, background is typically removed by recording the spectrum of the source blocking the light from the sample arm and then subtracting this background spectrum to every measurement.

Autocorrelation component appears near the zero OPL if the position of the reference mirror is such that  $(z_{S_n} - z_{S_m}) \ll (z_R - z_{S_n})$ , and this way it is possible to omit this artifact, but a more direct solution is to adjust the reference reflectivity to ensure that amplitude of cross-correlation terms are much higher than amplitude of auto-correlation terms.

Sensitivity improvement in FDOCT with respect to TDOCT arises from the fact that interference for all depths are captured simultaneously, considering that the signal is acquired in  $k$  space and it is known that each value in frequency domain contributes to all values in spatial domain. In FDOCT, there are two approaches to measure the spectral interferogram. Most intuitive way is to use a digital spectrometer as detector as shown in Figure 2.4, which provides the intensity signal as a function of wavenumber  $I_D(k)$  in a single measurement, and it is known as spectral domain OCT (SDOCT). Digital spectrometers are composed of a linear camera and an optical system that separates the spectral components of input light in such way that each pixel of the detector captures the intensity of a portion of the spectrum. Imaging speed in SDOCT is limited by acquisition rate of the linear camera and typical A-line rates are between 2 – 50 kHz.

The second approach in FDOCT is to use a tunable light source with a narrow spectrum and to acquire the interference signal  $I_D(k)$  with a single-element photodetector while the central emission wavenumber  $k$  of the light source is swept among

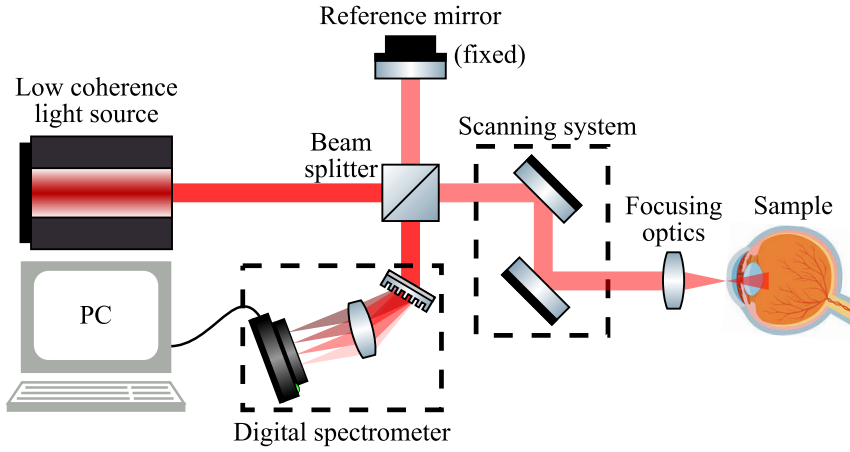


Figure 2.4: Schematic of a generic SDOCT setup based on a Michelson interferometer, where axial scan is obtained by computing the Fourier transform of the spectral interferogram acquired with a digital spectrometer.

a broad spectrum, and it is known as wavelength-swept source OCT (SSOCT). It is also referred as optical frequency domain imaging (OFDI) instead of low coherence interferometry given that, in rigorous terms, instantaneous emission of the tunable light source is considered coherent. OFDI achieves the highest imaging speed in OCT, presenting A-line rates up to 200 kHz, and it is limited by the sweeping rate of the light source. Hereafter, OFDI is used to refer to the imaging technique and SSOCT is used to refer to the OCT systems used for OFDI. A more detailed description of SSOCT systems is provided below, because this is the one of interest for this work.

### 2.1.5. Optical frequency domain imaging

Operation of OFDI is grounded on the fact that OPL and wavenumber are conjugate variables. In low coherence interferometry, interference is acquired illuminating the sample with light spanning several wavenumbers while OPL is scanned. In the alternative scenario, interference corresponding to all OPLs at the same time is acquired while illuminating the sample with light spanning a single wavenumber that is scanned, and this is the principle of operation of OFDI. Then, a Fourier transform of the signal in spectral domain yields the depth-dependent signal.

Detection scheme in OFDI employs a single-element detector, allowing higher A-line rates than in SDOCT systems that are limited by the acquisition rate of the linear camera, which is composed of multiple pixels. Increasing imaging speed reduces motion artifacts when imaging *in vivo* and allows larger scans in limited time. Tunable light sources are available in the 1–1.3  $\mu\text{m}$  wavelength range, where cameras technology is not well established, hence SSOCT systems are used commonly in the 1–1.3  $\mu\text{m}$  range that serves for multiple medical applications and SDOCT in the

complementary 0.85–1  $\mu\text{m}$  range used mainly in ophthalmology.

The most relevant specifications of tunable light sources in SSOCT are repetition rate, instantaneous linewidth  $\delta\lambda$ , tunable range  $\Delta\lambda$  and tuning curve  $k_i(t)$ . Axial resolution is determined by central wavelength of emission  $\lambda_c$  and tunable range  $\Delta\lambda$  equally to Eq. 2.1,  $\delta_z = \frac{2\ln 2}{\pi} \frac{\lambda_c^2}{\Delta\lambda}$ , thus it is independent of instantaneous linewidth. Instead, the depth range  $\Delta z$  observed within a single A-line is determined by the instantaneous linewidth as

$$\Delta z = \frac{\lambda_c^2}{4\delta\lambda} \quad (2.8)$$

and is independent of tunable range. Note that central wavelength mediate in both parameters. As a numerical example, a tunable light source with instantaneous linewidth  $\delta\lambda = 0.1 \text{ nm}$  and tunable range  $\Delta\lambda = 125 \text{ nm}$  centered at  $\lambda_c = 1.3 \mu\text{m}$  provides  $6 \mu\text{m}$  axial resolution along 4.2 mm depth range. The same light source but with central wavelength  $\lambda_c = 860 \text{ nm}$  provides  $2.7 \mu\text{m}$  axial resolution over 2.15 mm.

Tunable curve  $k_i(t)$  determines the instantaneous wavenumber as a function of time  $t$ . Ideally, this is a linear curve  $k_i(t) = k_0 + k_s t$  where  $k_0$  is the initial wavenumber and  $k_s$  is the wavenumber step between consecutive instantaneous wavenumbers. In practice,  $k_i(t)$  is a non-linear function of time and thus linearization is required, typically performed on post-processing prior to computing the Fourier transform of the spectral interferogram, otherwise, artifacts appear degrading axial resolution.

Development of SSOCT systems have inherited technology from optical communications in the near infrared spectrum that employs similar optical components such as tunable laser sources, optical fiber and detectors. In that sense, there are multiple types of tunable light sources relying on different principles of operations, but currently the development of fast, stable, linear, low-cost tunable light sources is a very active area of research.

Lasers are optical oscillators comprising a gain medium that is pumped optically or electrically to amplify light by stimulated emission, and an optical cavity that gives coherent optical feedback for laser oscillations []. Semiconductor optical amplifier (SOA) is a gain medium widely used for tunable lasers because they offer a high gain in a broad bandwidth, a rapidly response time, in the picosecond scale, and a wide range of gain center wavelengths depending on the semiconductor materials. One way to construct tunable lasers is to incorporate in the basic laser instrumentation an internal or external scanning filter to select the central wavelength of the instantaneous emission. One of the first approaches developed for OCT applications was tunable laser based on scanning filter using a polygonal mirror and to date this is widespread in research and medical systems. Polygon-based tunable lasers offer

high sweep rate in a wide tuning range with narrow linewidth, ideal features for OCT imaging.

In polygon-based lasers, the optical cavity includes a diffraction grating, a telescope and a rotating polygonal mirror with tens of facets. Light emitted by a SOA within a broad spectrum is reflected by the diffraction grating in such way that there is an angular separation of spectral components. Light is relayed to the polygonal mirror through the telescope, and only the spectral component incident perpendicular to the mirror surface is reflected back to the grating and then to the SOA, proving a coherent light feedback. Rotation of the polygonal mirror changes surface angle and therefore the instantaneous spectral component that has perpendicular incidence also changes. Drawbacks of this scanning filter approach is that polygonal mirror is a relatively bulky and moving part.

Figure 2.5 illustrates an optic fiber-based SSOCT system using a polygon-based tunable laser. Light from the tunable laser is delivered to an optic fiber beam splitter that divides the light into the sample and reference arms, then, reflected light from both produce interference that is detected by a photodetector and digitized. In this scheme, balanced detection is illustrated using two detectors to subtract the background signal and thus suppressing excess noise. Moreover, SSOCT systems require a trigger signal to synchronize detector acquisition with rotation of the polygonal mirror. In the system of Fig. ??, the trigger signal is generated by a narrowband fiber Bragg grating (FBG) that reflects light of a specific wavelength, thus when the laser source emits this wavelength, the FBG reflects light generating a pulse that indicates the beginning of interferogram acquisition, performed using N analog-to-digital conversions (ADC) following a sample clock.

Compact tunable lasers have been possible with vertical cavity surface emitting lasers (VCSEL) in conjunction with a micro-electro-mechanical mirror system (MEMS) used to vary the cavity length of the VCSEL, thereby tuning the output wavelength. MEMS-VCSEL sources however have a limited tuning range and broad instantaneous linewidth although they are in current development to provide a powerful alternative to polygon-based sources []. In addition, current research focuses in developing akinetic tunable lasers to provide more robust and reliable light sources with the same or even better features of polygon-based sources [].

### 2.1.6. Phase stability in OCT configurations

Being an interferometric technique, OCT provides information of the *complex amplitude* of the light backscattered by the sample, and this includes phase and amplitude information. This is an important feature of OCT because the complex amplitude provides more information than the amplitude (or intensity) alone, enabling opera-

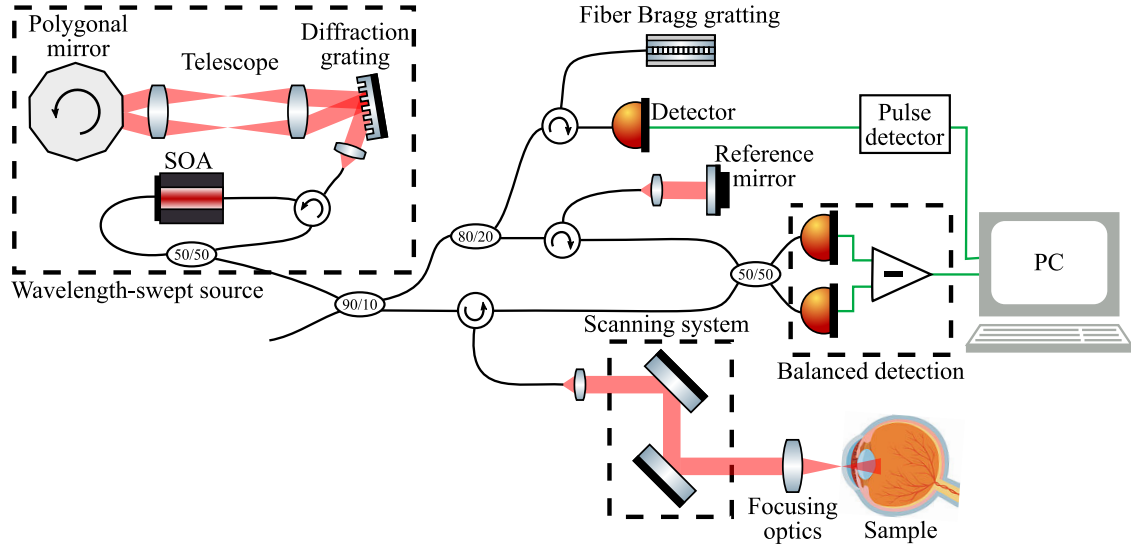


Figure 2.5: Schematic of a fiber-based SSOCT setup where the wavelength-swept source changes its instantaneous central wavelength in time due to the rotation of the polygonal mirror. A trigger signal to start the acquisition of the spectral interferogram is produced by the fiber Bragg grating that is designed to reflect a single wavelength, indicating the start of a sweep cycle of the light source.

tion of phase-resolved functional techniques and phase-dependent post-processing.

In OCT, there are several undesired contributions to the phase that are considered as *phase noise*, arising from the system or from the sample, making development of phase-resolved OCT technology challenging. The ability of a system to provide repeatable phase measurements is known as *phase stability* and it exists when there is a constant phase relation between measurements, that is, when the phase difference between entirely correlated measurements is zero. In phase sensitive techniques like flowmetry, phase difference between successive measurements is directly related to the flow velocity, and phase stability is crucial because phase noise causing phase fluctuations adds spurious contribution to the calculation of the phase difference inducing errors in the velocity estimation.

Phase stability is greatly influenced by the configuration used for axial and transverse scan. In SDOCT, the parallel acquisition of the entire spectral interferogram within a single measurement ensures phase stability inside A-lines, thus axial axis is phase stable. In addition, the high repeatability of spectrometers ensure phase stability along successive A-lines measured at different times while scanning the beam in the sample, hence in principle SDOCT provides three-dimensional phase stability. However, there are two additional sources of phase noise in OCT, one induced by sample motion that is detailed in Section [?], and second is induced in the galvanometer scanning system, due to separation of the pivot position of each galvanometer mirror and the back focal plane of the scan lens that adds a phase off-

set depending on the instantaneous angle of the mirror. Although there is a physical limitation in positioning the pivot point of both galvanometers mirrors at the back focal length of the scan lens, precise alignment of one mirror would ensure phase stability along its corresponding lateral scan axis.

In SSOCT systems, achieving phase stability have been more challenging than in SDOCT because each component of the spectral interferogram is acquired sequentially in time and not in parallel like in a spectrometer. In principle, this is not a limitation if experimental conditions of the system during A-line acquisition do not change, but there is a particular issue in regard to the trigger signal that have a detriment effect in phase stability. SSOCT systems require a trigger signal to synchronize A-line acquisition with wavelength sweep of the light source, for instance using a Fiber Bragg grating like in Fig. 2.5. However, the fast sweeping cycle of the light source demand precise electronics to obtain a perfect synchronization, but in practice this is not the situation and there is a time delay or *jitter* in the sample clock for acquisition with respect to the trigger signal. as a consequence, acquisition starts arbitrarily within the sweep cycle of the light source.

A jitter in synchronization causes a shift  $\delta k$  in the acquired spectral interferogram, thus the measured signal is  $\tilde{I}_D(k) = I_D(k - \delta k)$ . Depth-dependent signal obtained as  $i_D(z) = \text{FT}_k\{\tilde{I}_D(k)\}$  results in

$$\begin{aligned}\tilde{i}_D(z) &= \text{FT}_k\{I_D(k - \delta k)\} \\ &= \text{FT}_k\{I_D(k)\}e^{-i2\pi z\delta k} \\ &= i_D(z)e^{-i2\pi z\delta k}\end{aligned}\quad (2.9)$$

being  $i_D(z) = \text{FT}_k\{I_D(k)\}$  the unmodified depth-dependent A-line. Note that effect of spectral shift only impacts the phase of the A-line by the factor  $e^{-i2\pi z\delta k}$  that represents a phase ramp with slope  $-2\pi\delta k$ , known as *phase jitter* noise, but the amplitude  $|\tilde{i}_D(z)| = |i_D(z)|$  remains unchanged, thereby traditional structural OCT image based on the intensity  $|\tilde{i}_D(z)|^2 = |i_D(z)|^2$  is not affected. The random behavior of jitter in synchronization causes that the spectral shift  $\delta k$  varies randomly between spectral interferograms, and this dramatically impacts phase stability in raster scan systems because A-lines are captured sequentially in time while displacing the beam in the sample plane, inducing spatially-varying phase-jitter noise.

An approach to avoid phase-jitter is the use of  $k$ -clocks that produce a sample clock linear in  $k$  using a Mach-Zehnder interferometer. In standard systems, signal acquisition is performed linearly in time with  $N$  ADC following an internal electronic sample clock. With a  $k$ -clock, ADC are performed linearly in  $k$  with certainty. Therefore, the use of a  $k$ -clock avoids phase-jitter because the uncertainty in trigger

signal is solved, at the same time that acquired signal is linear in  $k$  eliminating the need of signal linearization in post-processing. Although there are  $k$ -clocked SSOCT systems available, they are not widespread because the need of additional hardware, thus phase-jitter is a very common issue affecting standard research and medical OCT systems. However, even using a  $k$ -clock, SSOCT systems are sensitive to galvanometer and sample motion phase noise, affecting its phase stability.

In the previous descriptions, it is possible to note that phase stability is very limited in raster scan systems, whether SDOCT or SSOCT, because transverse scan is performed in time. Parallel acquisition of A-lines for different transverse location can be achieved with extended-field systems where light is projected onto the sample in an extended area. In line-field SDOCT (LF-SDOCT), the sample is illuminated with a line-shaped beam produced by a cylindrical lens and the linear detector in the digital spectrometer is replaced by a two-dimensional detector; one dimension correspond to the  $k$  space and the orthogonal dimension corresponds to the transverse fast scan axis. Hence, a single acquisition of the detector provides a B-scan view, and a single galvanometer is required to scan the beam along the slow scan axis providing three-dimensional images. Parallel acquisition along fast scan axis ensures phase stability *in vivo* in this axis as long as acquisition rate is relatively fast compared to the velocity of the sample motion, nonetheless, slow scan axis typically remains phase unstable.

TDOCT and SSOCT systems allow full field (FF) acquisition where the sample is illuminated with an extended collimated beam, the single-element detector is replaced by a two-dimensional detector and additional optical lenses are used to image the sample plane on the detector plane, hence a single axial scan provides an entire tomogram with volumetric phase stability, even *in vivo* if acquisition rate is relatively fast compared to the velocity of the sample motion. Figure 2.6 illustrates simple schematics of LF-SDOCT and FF-SSOCT systems.

Extended-field OCT systems are custom configurations used in particular scenarios, like in the CAC research area because they offer sufficient phase stability, but they are not widespread given that they have a more complex optical design including 2D detectors that are not well developed in terms of speed and sensitivity in the near-infrared range, but more importantly, they are more prone to multiple scattering. Scattered light in tissue can be divided into two components: single scattering and multiple scattering (MS), the former is the backscattered signal of interest in OCT and the latter is an undesired component arising from light that is scattered multiple times following random paths that reaches the detector, but it does not contribute direct information to the OCT signal due to its random properties. Raster scan systems have an intrinsic rejection to MS given because of confocal gating, that is, the focused beam scans a small region of the sample in a limited

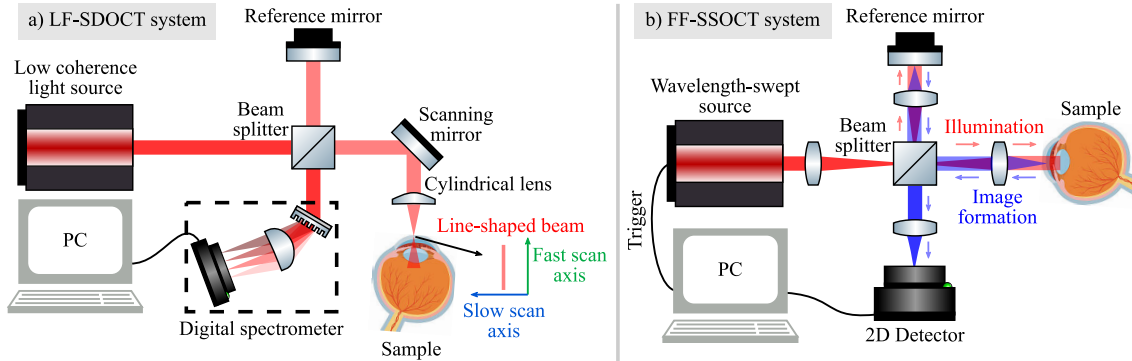


Figure 2.6: Schematic of generic a) LF-SDOCT setup for acquisition of a B-scan in a single detector shot and b) FF-SSOCT setup for acquisition of a tomogram in a single cycle of the wavelength-swept source. Red path illustrates the illumination beam and blue path the image formation on detector plane for a point.

field of view (FoV). Extended detection is more prone to collect MS photons given that the FoV during each measurement is larger.

## 2.2. Modelling the acquisition of the complex OCT signal

In previous section, OCT experiment was described and analyzed from an interference perspective to derive the acquisition of axial scan that provides the depth-dependent signal by means of optical interferometry, however, this corresponds to the complex field of backscattered light by the sample but the ultimate aim is to obtain the *scattering potential* of the sample denoted as  $\eta$  that gives information of sample structure. In other words, in OCT the optical beam probe is used to measure  $\eta$  indirectly; the acquired signal contains the sample scattering information as well as the effect of the optical system. In the ideal situation, the effect of the optical system is not significant and the measured signal is directly related to  $\eta$ . This is the case of systems with aberration-free optical beams where imaging is diffraction-limited and the theoretical lateral resolution is achievable, but in the presence of aberrations, the optical field is distorted and effective lateral resolution is reduced.

Scattering theory can be used to derive a model of the imaging formation process that relates the measured signal with the sample structure, known as *forward model*. Inversion of the forward model results in the *inverse scattering model* that allows to recover an approximate sample structure from the backscattering signal. Solutions to the inverse scattering model brought the development of computational techniques for aberration correction of OCT tomograms. In this section, the forward model is presented and subsequent section surveys solutions to the inverse scattering model to correct aberrations in post-processing.

### 2.2.1. Confocal gating for lateral scan in OCT

In raster scan systems, the transverse scan is performed using confocal gating resulting from the distribution of the focused beam. When light is focused on the sample plane, the illuminated cross-sectional area defines the lateral resolution and it can be given in terms of the beam diameter. Typically, at the back focal length of the optical system, the probe beam with central wavelength  $\lambda_c$  is a Gaussian beam with a  $1/e^2$ -diameter  $D$ , and after the optical system, light is focused at the front focal length  $f$  in a spot with a  $1/e^2$ -radius  $w_0$  that defines the diffraction-limited lateral resolution  $\delta x$

$$\delta x = 2w_0 = \frac{4\lambda_c}{\pi} \frac{f}{D}, \quad (2.10)$$

where  $\frac{D}{2f} = \text{NA}$  is the numerical aperture of the optical system, and its inverse relation to  $\delta x$  means that fine transverse resolution can be obtained in high NA systems that produce small focused spots. Due to convergence and divergence, the  $1/e^2$ -radius  $w(z)$  of the focusing beam varies with depth  $z$ , and setting  $z = 0$  at the front focal plane,  $w(z)$  can be expressed as

$$w(z) = w_0 \sqrt{1 + \left( \frac{z\lambda_c}{\pi w_0^2 n} \right)^2} \quad (2.11)$$

where  $n$  is the refractive index of the propagating medium.

Eq. 2.11 shows that diffraction-limited resolution is only possible at the focal plane ( $z = 0$ ) and is degraded for other planes. However, for distances  $z$  relatively close to the focal plane, change of spot size is relatively small. The confocal parameter  $b$  is defined as the distance within which the spot size is smaller than  $\sqrt{2}\delta x$  and thus resolution can be considered as nearly constant, and it is given by

$$b = 2z_R = \frac{\pi\delta x^2}{\lambda} \quad (2.12)$$

where  $z_R$  is known as the Rayleigh range. Confocal parameter defines the region where defocus is negligible and is also referred to as depth of field (DoF). It is proportional to the beam spot size squared and this establishes the lateral-resolution–DoF trade-off; high NA systems provides high resolution images in a limited DoF whereas low NA systems provides low resolution images in an extended DoF. In general, OCT systems employs low NA (between 0.01 and 0.15) to obtain tomograms with nearly focal resolution throughout the whole axial scan and this have limited transverse resolution in OCT to  $\sim > 10 \mu\text{m}$ , although in certain applications high

NA systems are used and known as optical coherence microscopy (OCM) ??.

To illustrate confocal gating and its relation to numerical aperture, Figure 2.7a) shows the focused beam produced by two optical systems in different NA regimes, for a wavelength  $\lambda_c = 1 \mu\text{m}$ . Low NA system (red) produces a large spot size but its size remains nearly constant along a large DoF. In contrast, the second system (blue) has a NA four times larger producing a spot size four times smaller but its size increases abruptly reducing the DoF by  $4^2$  times. Fig. 2.7b) shows the square relationship between confocal parameter and transverse resolution, indicating the corresponding values of the NA used in Fig. 2.7a).

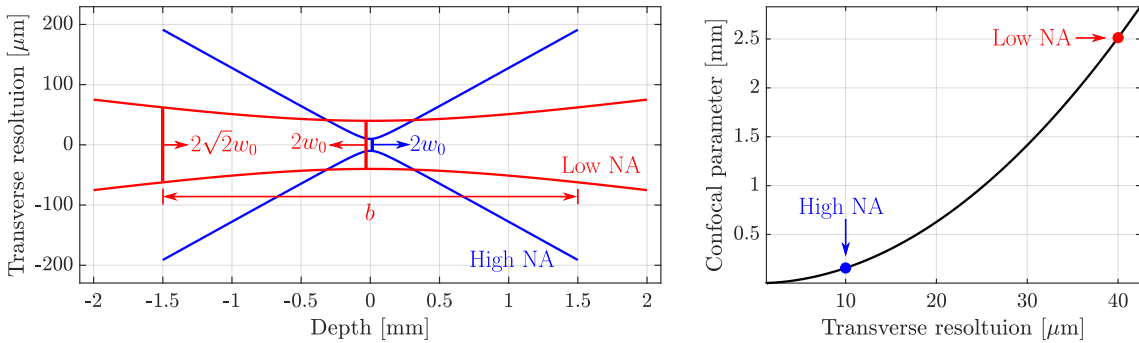


Figure 2.7: Illustration of confocal gating for light with  $\lambda_c = 1 \mu\text{m}$ . a) Focused beam produced by two optical systems with relatively low and high NA. b) Relation between confocal parameter and transverse resolution.

With this qualitative description of the resolution-DoF-trade-off, it is possible now to analyze how this impacts the acquired complex signal.

### 2.2.2. Forward model

This section presents the forward model (FM) that relates the measured OCT signal to the sample structure considering the effect of the optical system using a model for the image formation process. In the FM, the propagation of the Gaussian probe beam is taking into consideration to derive an expression for the interference signal that also considers the effect of confocal scan. From Fourier optics theory, the acquired signal  $S(x, y; k)$  for wavenumber  $k$  at transverse coordinates  $(x, y)$  can be modelled as  $S(x, y; k) = h(x, y, z; k) \otimes \eta(x, y, z)$ , that is the convolution (denoted by  $\otimes$ ) of the system point-spread function (PSF)  $h(x, y, z; k)$  with the scattering potential of the sample  $\eta(x, y, z)$  ??,

$$S(x, y; k) = \iiint h(x - x', y - y', z'; k) \eta(x', y', z') dx' dy' dz' \quad (2.13)$$

where the integration over  $z'$  indicates that light is captured simultaneously for all depths, as occurs in Fourier domain detection. The PSF  $h(x, y, z; k)$  can be expressed as the product of the incident and detection complex probe beams  $g_i(x, y, z; k)$  and  $g_d(x, y, z; k)$  respectively, but given that OCT is based on a reflection (double-pass) geometry, the incident and collection beams are identical to  $g(x, y, z; k)$ , hence

$$h(x, y, z; k) = k^2 |A(k)|^2 g^2(-x, -y, z; k), \quad (2.14)$$

where  $|A(k)|^2$  is the power spectral density and the inversion of lateral coordinates  $(x, y)$  is due to the reflection geometry.

To derive a model for the probe beam  $g(x, y, z; k)$ , consider that the beam at the focal plane  $z = z_0$  and transverse coordinate  $\mathbf{r}_0 = (x, y, z_0)$  is a normalized Gaussian probe beam

$$g_0(\mathbf{r}_0; k) = \frac{1}{2\pi w_0^2(k)} e^{-\mathbf{r}_0^2/[2w_0^2(k)]}, \quad (2.15)$$

with waist radius  $w_0(k) = \alpha/k$  for wavenumber  $k$  and  $\alpha = \pi/\text{NA}$ . Using plane-wave decomposition with transverse frequency coordinate  $\mathbf{q} = (q_x, q_y, 0)$ , the beam at  $\mathbf{r} = (x, y, z)$  in any plane  $z$  is described as

$$g(\mathbf{r}; k) = \frac{1}{(2\pi)^2} \iint e^{i(z-z_0)\sqrt{k^2-q^2}} e^{-q^2\alpha^2/2k^2} e^{i\mathbf{q}\cdot\mathbf{r}} d^2q \quad (2.16)$$

Using Eqs. 2.13 and 2.14, it is possible to model the measured OCT interference signal taking into consideration the beam distribution, as explained in detail in Ref. ??, by means of the expression

$$S(\mathbf{r}'; k) = \frac{A(k)}{(2\pi)^2 k} \iiint f^2(\mathbf{r} - \mathbf{r}'; k) \eta(\mathbf{r}) d^2r dz, \quad (2.17)$$

where the term  $f^2(\mathbf{r}; k)$  is given by

$$f^2(\mathbf{r}; k) = \frac{1}{8\pi^2} \left( \frac{\alpha^2}{k^2} + \frac{iz}{k} \right)^{-1} \iint e^{-q^2\alpha^2/4k^2} e^{iz\sqrt{4k^2-q^2}} e^{-i\mathbf{q}\cdot\mathbf{r}} d^2q. \quad (2.18)$$

To understand Eq. 2.17, note that  $\mathbf{r}' = (x', y', z_0)$  is the instantaneous transverse position of the probe beam during a raster scan. The signal  $S(\mathbf{r}', k)$  measured for the instantaneous wavenumber  $k$  when the beam is located at the instantaneous position  $\mathbf{r}'$  is the contribution of all point scatterers in the sample weighted by the function  $f^2(\mathbf{r} - \mathbf{r}'; k)$ , and scaled by a value proportional to the light source intensity

for  $k$ ,  $A(k)$ . Finally, a Fourier transform of  $S(\mathbf{r}'; k)$  with respect to  $k$  yields the depth-dependent signal  $S(\mathbf{r}', z)$ . In regard to  $f^2(\mathbf{r} - \mathbf{r}'; k)$ , the factor  $\frac{1}{8\pi^2} \left( \frac{\alpha^2}{k^2} + \frac{iz}{k} \right)^{-1}$  can be considered as a depth-dependent signal-loss factor that describes the signal reduction far from the focal plane,  $e^{-q^2\alpha^2/4k^2}$  is related to the Fourier spectrum of the Gaussian beam, the factor  $e^{iz\sqrt{4k^2-q^2}}$  encompasses both the interference and the PSF broadening effect, responsible of the signal blurring, and last factor  $e^{-i\mathbf{q}\cdot\mathbf{r}}$  is the Fourier transform kernel as Eq. 2.18 is actually a Fourier integral.

To illustrate the forward model, Figure 2.8 shows an example of an OCT B-scan image simulated using Eq. 2.17. For this purpose, a collection of 128 point scatterers with random positions where defined within an axial and lateral field of view (FoV) of  $820 \times 450 \mu\text{m}$  as depicted in Fig. 2.8a). The light source have  $\Delta\lambda = 150 \text{ nm}$  and  $\lambda_c = 1.310 \mu\text{m}$  providing an axial resolution of  $\delta z = 5 \mu\text{m}$ . The numerical aperture is  $\text{NA} = 0.25$ , a relatively high value, resulting in lateral resolution  $\delta x = 5 \mu\text{m}$  throughout a depth of field of  $b = 30 \mu\text{m}$ , producing the Gaussian beam shown in Fig. 2.8b), where the focal plane is clearly located at  $z_0 = 0$ . To generate the simulated OCT image shown in Fig. 2.8c), the location of the Gaussian beam is changed iteratively, and in each location the contribution of all point scatterers weighted by  $f^2(\mathbf{r} - \mathbf{r}'; k)$  is computed using Eq. 2.17. At the  $n$ -th iteration, the location of the Gaussian beam is  $\mathbf{r}'_m = (ndx - \frac{\Delta x}{2}, 0, z_0)$ , where  $\Delta x$  is the lateral FoV and  $dx = 1.75 \mu\text{m}$  is the sampling step which is smaller than Nyquist sampling  $\delta x/2$ .

The lateral blurring due to the convergence and divergence of the probe beam is evident in Fig. 2.8c). Resolution within the confocal region marked as  $b$  is diffraction-limited, so that point scatterers inside  $b$  appear in focus, like the one inside the red rectangle, contrary to point scatterers away from the focal plane that appear blurred in the lateral axis as a consequence of beam size increase, such as the one in the yellow rectangle. Note that superposition of signal from different point scatterers cause interference, like the two superimposed points in the white rectangle. When the number of point scatterers increases, random interference occurs and this phenomenon gives rise to speckle [].

It is important to remark that confocal effect is not restricted to the lateral axis. The factor  $e^{iz\sqrt{4k^2-q^2}}$  in Eq. (2.18) can be written as  $e^{izq_z(k,\mathbf{q})}$ , where  $q_z = \sqrt{4k^2 - q^2}$  is the axial frequency coordinate of the object. Because  $q_z$  encompasses  $k$  and  $\mathbf{q}$ , there is a mixing of the lateral and axial information that produce a coordinate warping, from the sample frequency coordinates  $(q_x, q_y, q_z)$  to the signal frequency coordinates  $(q_x, q_y, k)$ . As a consequence, there is an apparent object curvature away from the focal plane as observed in the yellow inset of Fig. 2.8c). The signal warping occurs because the object axial frequency component  $q_z$  is not measure directly but through the light wavenumber  $k$ . In other words, the object frequency content

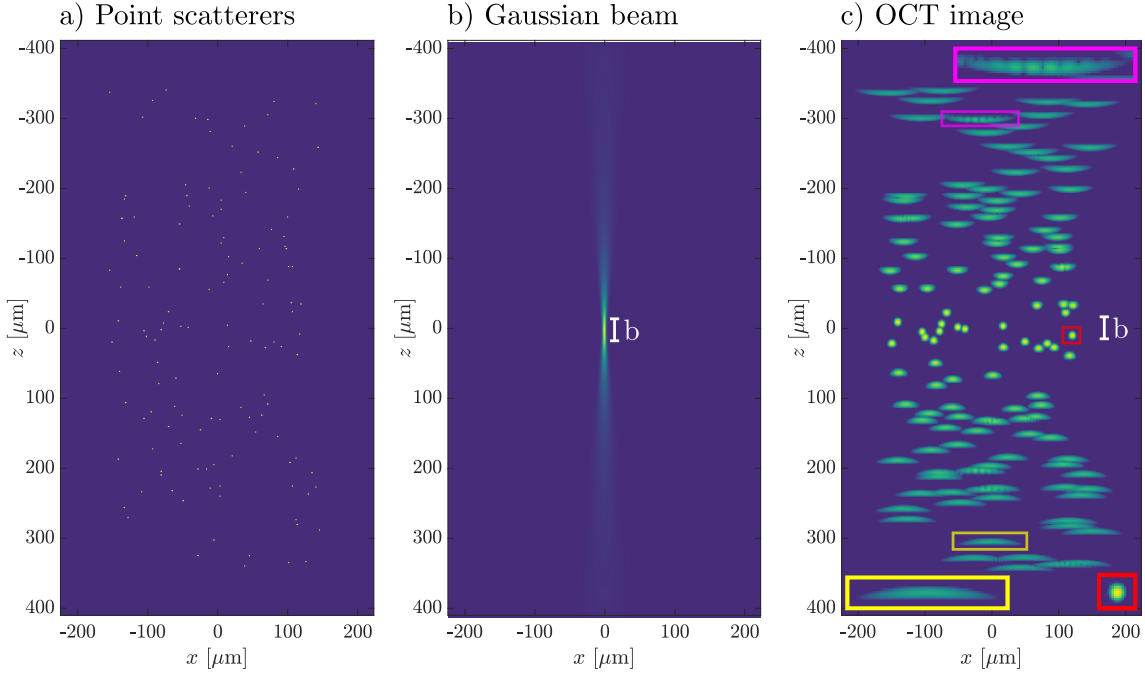


Figure 2.8: Simulation of an OCT image in high-NA regime. a) Sample consisting of randomly located point scatterers, b) Gaussian beam of the system with  $\text{NA} = 0.25$  and c) OCT image simulated using the forward model, displayed in logarithmic scale.

is in the  $(q_x, q_y, q_z)$  space, but the measured signal is the  $(q_x, q_y, \frac{1}{2}\sqrt{q_x^2 + q_y^2 + q_z^2})$  space. This phenomenon is significant in high NA regime, and for low-NA regime an approximation can be made to simplify the FM as will be discussed in the next section.

For a comparison between high and low NA regimes, Figure 2.9 illustrates the result of imaging the same sample of Fig. 2.8a) changing the NA to 0.1, resulting in a lateral resolution of  $12.5 \mu\text{m}$  throughout a depth of field of  $190 \mu\text{m}$ . The Gaussian beam produced with this NA have a more constant beam size along depth, as shown in Fig. 2.9b) in contrast to the previous NA used for Fig. 2.8b). As a result, resolution loss away from the focal plane is less abrupt, at the expense of presenting a larger diffraction-limited spot size.

### 2.3. Refocusing and computational aberration correction techniques in OCT

In the FM of Eq. 2.17, the OCT signal  $S$  is given by the sample potential  $\eta$  modified by the system function  $f^2$ . From this model, it is possible to computationally obtain an approximate scattering sample potential  $\tilde{\eta}$  by correcting the undesired effects

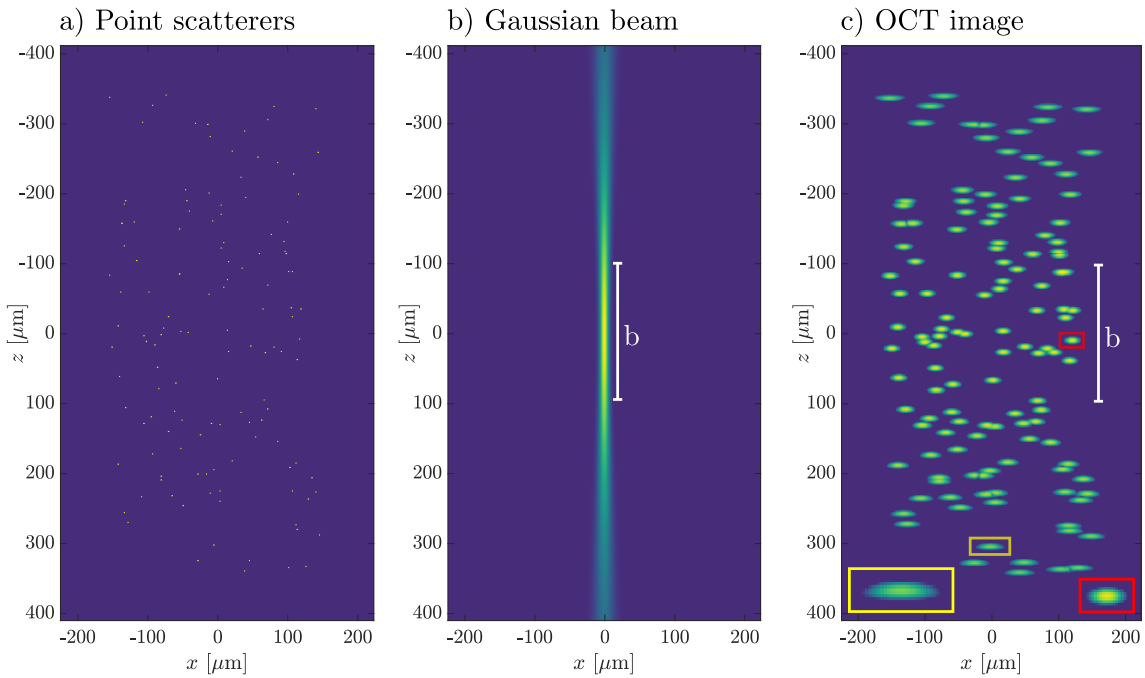


Figure 2.9: Simulation of an OCT image in low-NA regime. a) Sample consisting of randomly located point scatterers, b) Gaussian beam of the system with NA=0.1 and c) OCT image simulated using the forward model, displayed in logarithmic scale.

present in the acquired signal  $S$ , that so far is only defocus due to the beam propagation, but additional aberrations may also be considered with further extensions presented below. There are several computational aberration correction techniques, some are oriented to correct for defocus to provide focal resolution throughout all depths, and others are oriented to correct for other types of aberrations that depend on the specific imaging system or even on the sample itself, in addition to defocus, and they are explained in the following sections.

To retrieve an approximate scattering sample potential from the acquired signal it is necessary to invert the forward model, what is known as an inverse scattering problem. In simple words, the FM gives the backscattering signal produced for a given scattering potential, while the inverse model gives the scattering potential that produced a given backscattering signal, and the latter is the interest in CAC.

For the derivation of CAC techniques, it is convenient to introduce the forward model in Fourier domain. To do so, the convolution theorem can be used to rewrite Eq.(2.13) as

$$\hat{S}(q_x, q_y; k) = \int \hat{h}(q_x, q_y, z'; k) \hat{\eta}(q_x, q_y, z') dz' \quad (2.19)$$

where  $\hat{S}(q_x, q_y; k) = \text{FT}_{x,y}\{S(x, y; k)\}$ ,  $\hat{h}(q_x, q_y, z; k) = \text{FT}_{x,y}\{h(x, y, z; k)\}$  is the depth-dependent frequency response of the PSF, and  $\hat{\eta}(q_x, q_y, z) = \text{FT}_{x,y}\{\eta(x, y, z)\}$ .

Using an asymptotic approximation for the far-from-focus and near-focus cases ??, Eq. (2.19) can be simplified to

$$\hat{S}(q_x, q_y; k) = H(q_x, q_y; k) \int \hat{\eta}(q_x, q_y, z') e^{iz' \sqrt{4k^2 - q^2}} dz' \quad (2.20)$$

where  $H(q_x, q_y; k)$  is the space-invariant axial and lateral frequency response of the PSF, that is directly related to the optical transfer function of the system. In Eq.(2.19), a Gaussian beam is not assumed, contrary to the derivation of the FM in Eq. (2.17), so that  $H(q_x, q_y; k)$  is a general function that may describe any aberration and not only defocus. Computational aberration correction makes use of the FM in frequency domain to reconstruct an approximate sample scattering potential. In the notation used here, the tilde accent  $\sim$  is used to denote that a quantity is an numerical estimation of the true quantity. For instance  $\tilde{\eta}$  is an estimation of  $\eta$  using any of the CAC models presented above.

### 2.3.1. Interferometric synthetic aperture microscopy

Interferometric synthetic aperture microscopy (ISAM) is a solution to the inverse scattering problem in OCT, and actually it is very similar to procedures used in synthetic aperture radar (SAR) and from this similarly arises the name ISAM. Eq. (2.20) can be considered as a Fourier integral with conjugate coordinates  $z'$  and  $q_z = \sqrt{4k^2 - q^2}$ , thus it is possible to write

$$\hat{S}(q_x, q_y; k) = H(q_x, q_y; k) \hat{\eta}(q_x, q_y, q_z) \quad (2.21)$$

where  $\hat{\eta} = \text{FT}_{x,y,z}\{\eta(x, y, z)\}$  is the 3D Fourier transform of the sample scattering potential. Eq. 2.21 is a one-to-one mapping between  $\hat{S}$  and  $\hat{\eta}$ , contrary to convolution equation that is an all-to-all mapping between  $S$  and  $\eta$ . The principle of operation of ISAM is to re-sample the Fourier spectrum of the acquired signal  $S(x, y; k)$  in order to revert the coordinate warping, thereby the approximate scattering sample potential  $\tilde{\eta}(x, y, z)$  can be expressed as

$$\tilde{\eta}(x, y, z) = \frac{1}{\rho(z)} \text{FT}_{q_x, q_y, q_z}^{-1} \left\{ [H^{-1}(q_x, q_y; k) \hat{S}(q_x, q_y; k)] \Big|_{k=\frac{1}{2}\sqrt{q_x^2 + q_y^2 + q_z^2}} \right\}. \quad (2.22)$$

where  $\rho(z) = -1/z$  countervails signal loss when far from focus. Eq. 2.22 consist in several steps; 1) computing the Fourier transform of the acquired signal along transverse spatial coordinates, 2) re-maping coordinates from  $k$  to  $q_z$  using the relation

$k = \frac{1}{2}\sqrt{q_x^2 + q_y^2 + q_z^2}$ , known as the Stolt mapping ??, and then 3) computing the three-dimensional inverse Fourier transform  $\text{FT}^{-1}\{\cdot\}$ . For ISAM, an ideal Gaussian beam is generally assumed, so that  $H^{-1}$  is a weighting factor that will not introduce significant image distortion, thus it is usually set to unity. Normalization using  $1/\rho(z)$  is not appropriate in practical terms to compensate for signal loss away from focal plane, thus it is commonly omitted or replaced with other depth normalization function. ISAM reconstruction is illustrated in Figure ?? for the high-NA case of the simulated data in Fig. 2.8. The ISAM reconstruction shown in Fig. ??c) exhibit diffraction-limited resolution throughout all depths, and the major drawback present is the signal reduction, noticeable in points far from focal plane appearing dimmer than those in the focal plane.

ISAM, first proposed by Ralston et al. ??, has been used widely in the OCT community specially in high-resolution imaging where DoF is greatly reduced and computational correction of defocus is a key tool to extended the DoF ??, being the signal loss the major constrain. Extensions have been made to different imaging geometries and functional imaging, such as rotationally-scanned ISAM for endoscopic OCT ??, and polarization-sensitive ISAM ??.. Furthermore, the development of ISAM have enable real-time in vivo visualization ??.

### 2.3.2. Digital refocusing

ISAM reconstruction brings to focus all depths simultaneously, making use of the 3D frequency-content of the tomogram. In relatively low numerical aperture systems ( $\text{NA} < 0.15$ ) the re-sampling curve approximates a linear path which means that frequency content in not spread along depth, hence a 2D correction in the transverse plane determined for each plane  $z$  independently is sufficient. To isolate a single plane  $z_d$ , inverse Fourier transform along  $k$  of Eq.(2.20) is computed and evaluated at  $z = z_d$ ,

$$\hat{S}(q_x, q_y; z_d) = \int H(q_x, q_y; k) \int \hat{\eta}(q_x, q_y, z_d) e^{iz\sqrt{4k^2 - q^2}} e^{-i2z_d k} dz dk. \quad (2.23)$$

Replacing  $k = k_c + \Delta k$  with  $\Delta k$  the difference between  $k$  and central wavenumber  $k_c$ , the term  $(\Delta k/k_c)^2$  is relatively small enough to be neglected, allowing to express  $q_z = \sqrt{4k^2 - q^2}$  under the paraxial approximation as

$$q_z = 2k_c - \frac{q^2}{4k_c} + 2\Delta k. \quad (2.24)$$

Replacing  $q_z$  in Eq.(2.23), as well as using convolution theorem to rewrite Fourier

integral along  $k$ , it is possible to obtain

$$\begin{aligned}\hat{S}(q_x, q_y; z_d) &= \int H(q_x, q_y; k) \int \hat{\eta}(q_x, q_y, z_d) e^{iz(2k_c - q^2/4k_c + 2\Delta k)} e^{-i2z_d(k_c + \Delta k)} dz d\Delta k \\ &= \int H(q_x, q_y; k) \int \hat{\eta}(q_x, q_y, z_d) e^{i2(z - z_d)k_c} e^{-izq^2/4k_c} e^{i2(z - z_d)\Delta k} dz d\Delta k \\ &= H(q_x, q_y; z_d) \otimes \left[ \int \hat{\eta}(q_x, q_y, z_d) e^{i2(z - z_d)k_c} e^{-izq^2/4k_c} \delta(2z - 2z_d) dz \right] \\ &= H(q_x, q_y; z_d) \otimes \left[ \hat{\eta}(q_x, q_y, z_d) e^{-iz_dq^2/4k_c} \right]\end{aligned}\quad (2.25)$$

where the convolution is performed along axial axis. The depth-dependent part of  $H(q_x, q_y; z_d)$  is related to the axial PSF that can be approximated to a delta function, so that  $H(q_x, q_y; z) \propto H(q_x, q_y)\delta(z - z_d)$ , which can be replaced in Eq. (2.25) to obtain its inverse Fourier transform along  $\mathbf{q}$  as

$$S(x, y; z_d) = \text{FT}_{q_x, q_y}^{-1} \left\{ H(q_x, q_y) \hat{\eta}(q_x, q_y; z_d) e^{-iz_dq^2/4k_c} \right\}, \quad (2.26)$$

Eq. (2.26) is an expression with a form widely known in digital refocusing methods based on scalar diffraction models such as the Fresnel propagator [], where the exponential term is a quadratic phase term responsible of depth-varying defocus. A straightforward inversion of Eq. (2.26) provides an approximate refocused sample scattering potential by

$$\hat{\eta}(x, y; z_d) = \text{FT}_{q_x, q_y}^{-1} \left\{ H(q_x, q_y) \hat{S}(q_x, q_y; z_d) e^{iz_dq^2/4k_c} \right\}, \quad (2.27)$$

Similarly to ISAM, an ideal Gaussian beam can be assumed and  $H$  is set to unity. Although reconstruction using digital refocusing of Eq.(2.27) is not complex, there are conceptual differences with ISAM reconstruction. In digital refocusing, each depth is brought to focus independently, applying an appropriate quadratic phase term, whereas ISAM reconstruction restores the entire volume simultaneously re-sampling the signal in Fourier domain. More importantly, due to the paraxial approximation in Eq.(2.24), digital refocusing methods are valid only for low-NA regimes, where there is no coordinate warping that mixes lateral and axial information. Digital refocusing is illustrated in Figure 2.10 for the low-NA case of the simulated data in Fig.2.9, and note that digital refocused image of Fig. 2.10c) exhibit diffraction-limited resolution throughout all depth.

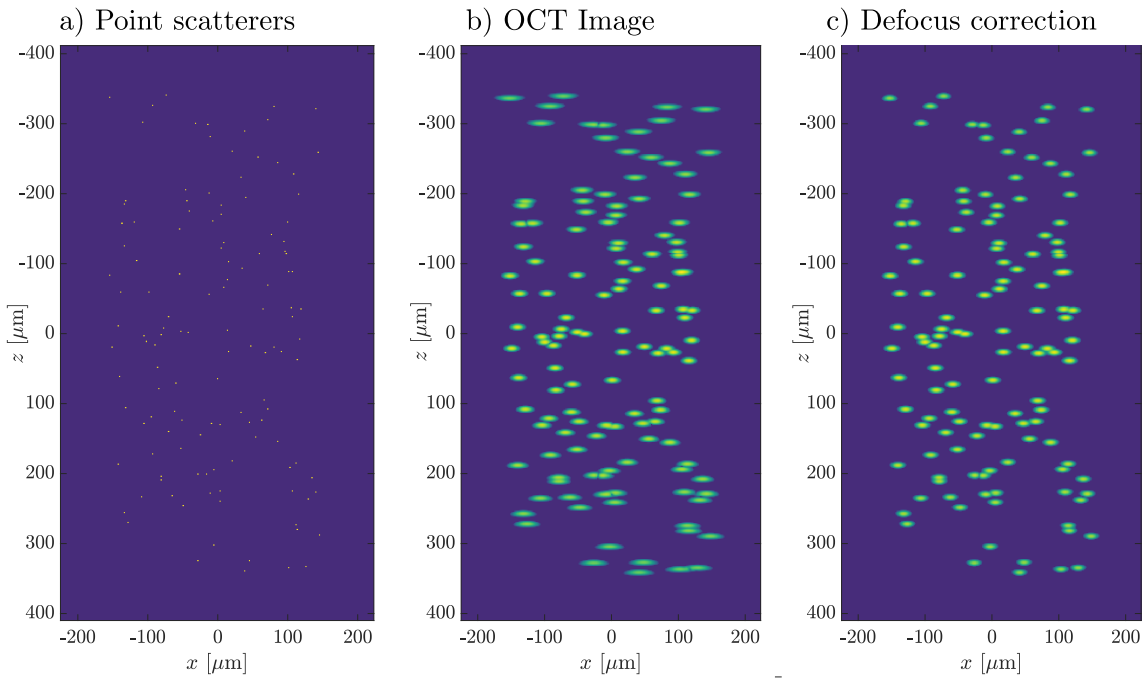


Figure 2.10: Illustration of digital refocusing. a) Sample consisting of randomly located point scatterers, b) OCT image simulated using the forward model, c) Digital refocused. b) and c) are displayed in logarithmic scale.

### 2.3.3. Computational adaptive optics

Aberrations are wavefront distortions with respect to a reference wavefront, affecting image quality in imaging techniques such as OCT. Several applications in OCT have benefited from aberration correction, whether using specific optical systems, hardware-based adaptive optics or computational adaptive optics. For instance, in retinal imaging, the probe beam is focused onto the retina using the optical system of the eye itself (cornea/lens) that may produce an distorted wavefront affecting image quality. In particular, the wavefront in high NA systems is more susceptible to be distorted by imperfections of the optical systems or even the sample itself.

Defocus introduced in the propagation of light is intrinsic to the Gaussian probe beam, for this reason, it is not considered as an optical aberration, in this case aberrations are wavefront deviations from the ideal wavefront of a Gaussian beam. This can be noted in Eq.(2.20), where defocus arises from the exponential term whereas wavefront distortions can be modelled by  $H(q_x, q_y; k)$  that is related to the effective generalized pupil of the optical system, resulting from the convolution of the illumination and detection generalized pupils, that are identical in OCT given the double-pass geometry.

Recalling the forward model in frequency domain, it is possible to invert Eq.(2.21)

to obtain an aberration-corrected OCT signal as

$$\tilde{\hat{S}}(q_x, q_y; k) = H^{-1}(q_x, q_y; k) \hat{S}(q_x, q_y; k). \quad (2.28)$$

where,  $H^{-1}(q_x, q_y; k)$  acts as a frequency filter, which depends on spatial frequency and spectral domains, therefore it can address chromatic aberrations []. Given the relatively narrow spectrum of the light sources used in OCT, in practical scenarios it is convenient to assume a  $k$ -independent filter  $H(q_x, q_y)$ , which is the same for all depths. In HAO, the correction filter  $H^{-1}(q_x, q_y)$  is applied directly in situ to compensate for the distortions of the Gaussian beam, but, because coordinate resampling is not included in this expression,  $\tilde{\hat{S}}(q_x, q_y; k)$  is an aberration-corrected signal rather than the sample scattering potential, it means that defocus will be present yet in the acquired images. To correct for defocus using HAO, a depth-dependent phase filter is necessary but it is not possible with current hardware such as deformable mirrors. In the case of CAO, the filter is applied in post-processing. ISAM or digital refocusing can be combined with aberration correction to obtain aberration-free images with focal resolution throughout all depths, namelely  $\tilde{\eta}(x, y, z)$ . For ISAM reconstruction, note that  $\tilde{\hat{S}}(q_x, q_y; k)$  is explicit in Eq.(2.22). For low-NA regime, the depth-invariant filter  $H(q_x, q_y; z_d)$  can be generalized in Eq.(2.27) to a depth-dependent filter  $H(q_x, q_y)$  that includes the exponential term, resulting in

$$\tilde{\eta}(x, y; z) = \text{FT}_{q_x, q_y}^{-1} \left\{ H^{-1}(q_x, q_y; z) \hat{S}(q_x, q_y; z) \right\}. \quad (2.29)$$

In this case, defocus is treated as an aberration contained in the correction filter.  $H^{-1}(q_x, q_y; z) = \Phi(q_x, q_z; z) e^{-i\phi(q_x, q_y; z)}$  is a complex filter comprising an amplitude factor  $\Phi(q_x, q_z; z)$  and a phase factor  $e^{-i\phi(q_x, q_y; z)}$ . Phase factor is explicit in Eq.(2.27) but the idea of CAO is to adaptively defined the phase factor based on the data rather than using the analytical expression, which only accounts for defocus and requires precise knowledge of physical quantities of the system, for instance, the location of the focal plane in the tomogram. The procedure to obtain an aberration-correction sample scattering potential using Eq.(2.29) is rather simple (note that it is a deconvolution in Fourier domain) the key point is to determine the appropriate correction filter. In CAO, the amplitude factor  $\Phi(q_x, q_z; z)$  is usually set to unity, because it does not produce a significant impact in image distortions, and a phase-only filter  $e^{-i\tilde{\phi}(q_x, q_y; z)}$  is used, where the phase  $\tilde{\phi}(q_x, q_y; z)$  is parameterized in terms of a polynomial basis, such as Zernike polynomials  $Z_i$  which are a convention for the description of optical aberrations []. Using a weighted sum with  $N$  Zernike

polynomials,  $\tilde{\phi}(q_x, q_y; z)$  is expressed as

$$\tilde{\phi}(q_x, q_y; z) = \sum_i^N Z_i \alpha_i(z_d), \quad (2.30)$$

with weights  $\alpha_i(z)$  that vary with depth. To determine  $\alpha_i(z)$ , there are two general approaches, optimization-based and sub-apertures correlation.

Sub-apertures correlation method proposed by Kumar et al. [] consists in measuring the local slope of the wavefront in the pupil/Fourier plane to determine the correction phase, emulating a Shack-Hartmann sensor. To do so, the Fourier transform of the acquire signal for each depth, namely  $\hat{S}(q_x, q_y; z)$ , is split into sub-apertures and the inverse Fourier transform of each sub-aperture is computed to yield images that will exhibit lower resolution and relative shifts between them. These images are cross-correlated to the image of a reference sub-aperture to measure the relative shifts, that is related to the local slope of the wavefront. Then, the local slopes are used to construct the phase correction, possibly using a decomposition like Eq.(2.30). The number of sub-apertures determines the degree of aberrations that can be corrected. For instance, splitting the pupil into two vertical and horizontal apertures enables defocus correction along the two scan axis. A large number of sub-apertures is desired to be able to correct for high-order aberrations, however, this leads to a significant resolution loss and increased image correlation error, which ultimately results in high errors in the determination of the correction phase.

Optimization-based CAO proposed by Addie et al. [] consists in finding the set of weights  $\alpha_i(z_d)$  that improves image quality as measured by a metric via optimization. The iterative operation of this procedure may increase computational time compared to sub-aperture based CAO, but it allows to straightforwardly include high-order aberrations by increasing the number of polynomials and weights used in the correction phase composition. Optimization-based CAO relies on the definition of a proper image quality metric, that ideally must have a minimum (or a maximum) when image aberrations are well compensated, being image sharpness metrics most used for this purpose since aberrations correction is supposed to improve sharpness. Shannon's entropy metric  $SE(I)$  of an image  $I_{m,n}$  with discrete indexes  $(m, n)$  and size  $M \times N$  is known to be minimal when aberrations are minimized, it has been used in the context of CAO in OCT, brought from SAR imaging, and is given by

$$SE(I) = \sum_i^M \sum_j^N \Gamma(\bar{I}_{i,j}), \quad (2.31)$$

where  $\Gamma(I) = -I \log I$  although different transformations can be used, and

$$\bar{I} = \left| \frac{I}{\sum_i^M \sum_j^N |I_{i,j}|} \right|^2 \quad (2.32)$$

is a normalized intensity image. Here,  $I_{m,n} = S(m, n; l)$  is the current  $l$ -th en face plane being compensated, where  $S(m, n; l)$  is the discrete counterpart of  $S(x, y; z)$ , with  $(m, n, l)$  denoting discrete indexes for  $(x, y, z)$ .

There are several image quality metrics that have been used in the context of other imaging modalities such as digital holography. For instance, Tamura's coefficient  $T = \sqrt{\frac{\sigma(I)}{\langle I \rangle}}$  is a measure of contrast, where  $\sigma(\cdot)$  is the standard deviation and  $\langle \cdot \rangle$  is the average value, and gradient-based metrics such as

$$G(I) = \sum_i^M \sum_j^N \sqrt{[I_{i,j} - I_{i-1,j}]^2 + [I_{i,j} - I_{i,j-1}]^2} \quad (2.33)$$

where  $I_{m,n} = |S(m, n; l)|^2$ . Image spatial frequency content metrics have been used in sensor-less HAO and eventually in CAO, and are based on the fact that mid-to high-frequency content of the complex amplitude should increase as resolution improves, i.e. when aberrations are minimized. One possible estimation is the ratio of energy within a band-pass frequency range to the total energy, expressed as

$$F(I) = \frac{\sum_i^M \sum_j^N |I_{i,j} B_{i,j}|^2}{\sum_i^M \sum_j^N |I_{i,j}|^2} \quad (2.34)$$

where  $I_{m,n} = \hat{S}(q_m, q_n; l)$ , being  $(q_m, q_n)$  discrete counterparts of  $(q_x, q_y)$ , and  $B_{m,n}$  is a band-pass filter with cut-off frequencies tuned to obtain a good performance.

Figure 2.11 illustrates the effect of aberrations in a simulated OCT image that was generated elsewhere [] with a probe beam waist diameter of  $10 \mu\text{m}$ . The tomogram consists of a large number of point scatterers distributed in the entire field of view as occurs in tissues, with similar index of refraction, producing speckle. In addition, point scatterers with a different index of refraction were added and arranged in a cylindrical shape along horizontal axis  $x$ , appearing as bright rectangles in the cross-sectional en face view of Fig.2.11a) located at the focal plane. Eq.(2.26) was used to induce defocus as if the en face plane of Fig.2.11a) were located at  $z = 200 \mu\text{m}$  from the focal plane, and defining the phase of  $H$  shown in Fig.2.11e), using Zernike polynomials  $Z_5$  and  $Z_7$  to induced astigmatism and coma aberrations with random magnitudes, resulting in the aberrated en face of Fig.2.11b), where

blurring is evident and consequently resolution loss.

Digital refocusing was applied to the aberrated en face using Eq.(2.27) setting  $H = 1$ , resulting in a refocused image with partial resolution improvement due to the presence of the remaining two aberrations deteriorating image quality. On the other hand, optimization-based CAO was applied to the aberrated en face using Eq.(2.29), describing the phase correction filter with  $Z_4$ ,  $Z_5$  and  $Z_7$ , being  $Z_4$  Zernike polynomial for defocus. Aberration-corrected en face of Fig.2.11d) exhibits focal resolution similar to the original en face, demonstrating the possibility of correcting defocus and additional aberrations using CAO.

To illustrate the behavior of image quality metric that is the basis of CAO, original en face of Fig.2.11a) was defocused using  $Z_4$  weighted by  $\alpha_4 = 17.8$  and then several corrected images were created with weights linearly varying between  $[-40, 20]$ . Figure 2.12 shows a plot of Shannon's entropy of the corrected image as a function of the correction weight  $\tilde{\alpha}_4$ , exhibiting a smooth behavior with a clear minimum at nearly  $\tilde{\alpha}_4 = -17.8$ , where the negative sign is because the correction phase term is the conjugate of the applied defocus term. Alongside Shannong's Entropy, there are six example en faces with different phase corrections, with the optimal en face enclosed in a red box, showing the best image quality among them.

Computational adaptive optics promises to be a powerful alternative to hardware-based adaptive optics that require very complex optical setups, specially in retinal imaging where the demand of cellular imaging increases for example in photoreceptors mosaic imaging ??.

There are two necessary requirements for computational aberration correction. Phase stability is so far the major requirement for computational aberration correction in OCT, but in addition lateral sampling must satisfy Nyquist sampling, i.e. lateral sampling must be equal or smaller than half the beam waist diameter, otherwise high-frequency content is not recovered properly and results will present distortions. In fact, Nyquist sampling is necessary in general for computational refocusing in almost any imaging technique, not only in OCT [].

### 2.3.4. Phase stability requirement

Computational techniques described previously rely upon accurate measurements of the complex amplitude information in order to guarantee a coherent aperture synthesis, necessary for aberration correction. Complex amplitude comprises amplitude and phase information, but phase is more susceptible to undesired fluctuations, hence reliable phase measurement is not a straightforward task due to experimental contains as explained in Section 2.1.6. In fact, first digital refocusing approaches in OCT were based on the intensity, but they provided very limited results given that

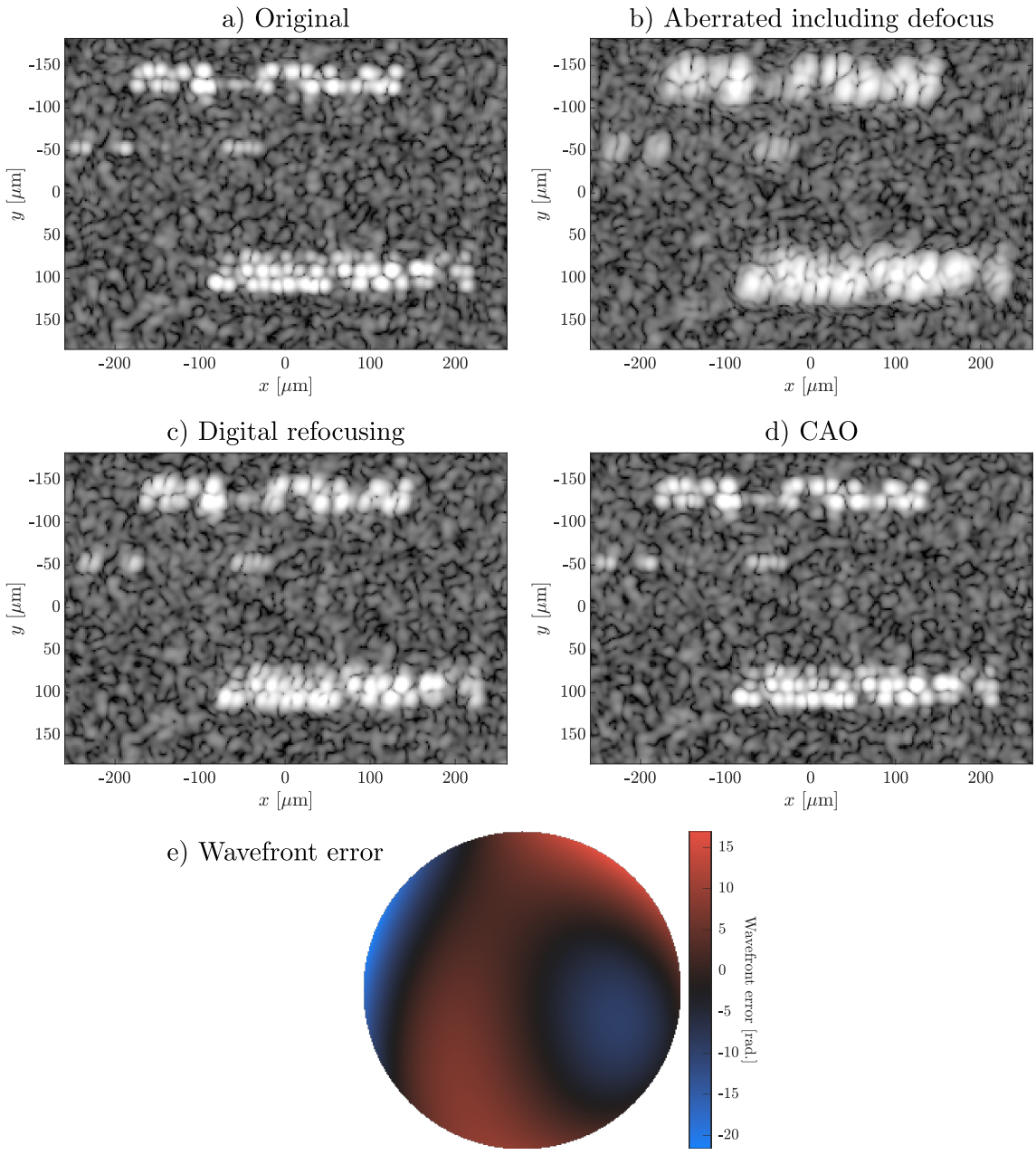


Figure 2.11: Illustration of computational adaptive optics. Simulated OCT en face image a) without and b) with aberrations and defocus, induced using the wavefront in e). Result of c) digital refocusing and d) computational adaptive optics. a)–d) are displayed in logarithm scale.

incoherent deconvolution ignores the phase information. Such initial approaches were designed to work with the intensity signal possibly because the lack of phase stable measurements in early OCT.

The aim of this section is to discuss phase stability requirement in the context of computational aberration correction. Phase stability is affected by phase noise that may arise from the system or the sample. Systems-induced phase noise sources,

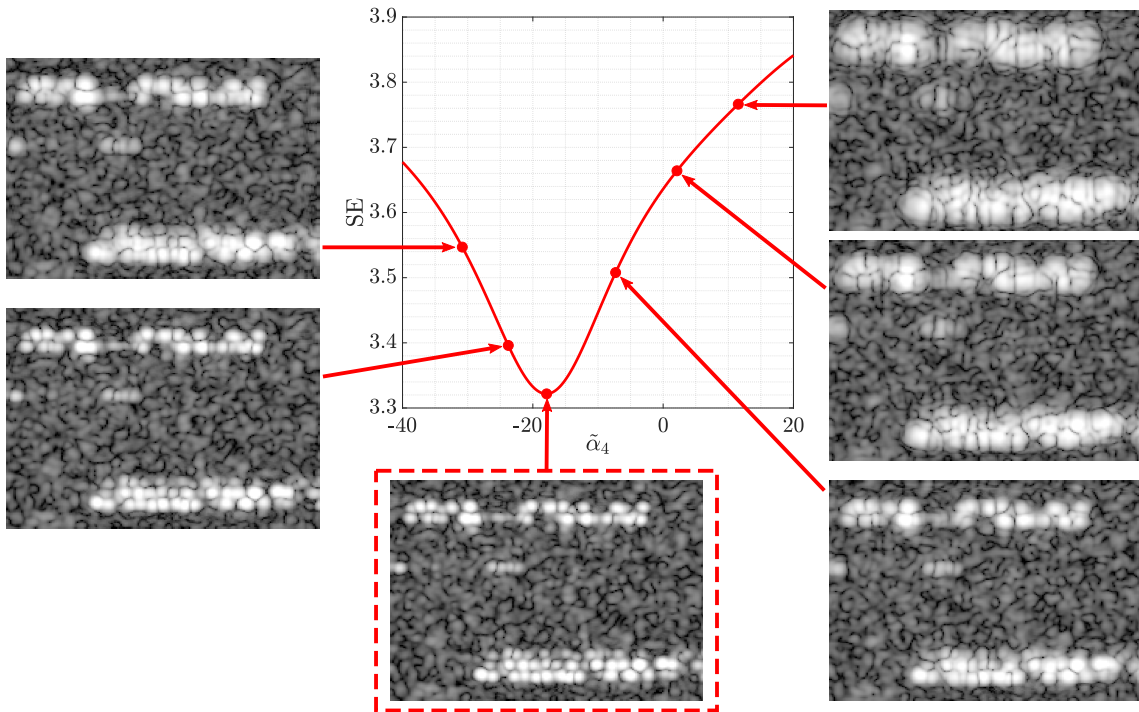


Figure 2.12: Illustration of Shannon's entropy metric to measure image sharpness of a defocused en face image corrected using Zernike polynomial  $Z_4$ . Plot shows the value of SE as a function of correction weight  $\tilde{\alpha}_4$ . Surrounding en faces images were corrected with different weights for a visual inspection of image quality. Optimal corrected image (on the red rectangle) corresponds to the minimum value of SE.

such as phase-jitter and galvanometer-induced phase noise, were explained in Section 2.1.6. On the other hand, sample-induced phase noise arises from sample motion, therefore it affects mainly *in vivo* imaging which is more prone to motion during signal acquisition than *ex vivo* imaging either global, such as involuntary motion of the subject, or internal such as blood flow in arteries.

Development of computational aberration correction has been grounded in SDOCT systems. For this reason, most significant phase instabilities induced by the system arise from the galvanometer scanners, which can be experimentally avoided in some cases, therefore, in this area, major attention have been put in sample motion-phase noise, which is the focus of following discussions.

Sample motion have two primary effects in the complex OCT signal; effective shift of the complex amplitude and phase-only jump. The former effect is rather intuitive, it is the displacement of apparent location of the signal in the tomogram, affecting both the amplitude and phase. The latter effect is an additional phase-only jump that is a consequence of Doppler effect, and actually it is used for functional imaging technique like flowmetry. Both effects have an impact in the phase of the tomogram and therefore they affect phase stability, but their influence vary

depending on system parameters. Effective complex amplitude shift scales with the spatial resolution of the system; the higher the resolution, the more susceptible the system may be to motion. In general, axial resolution is finer than lateral resolution, therefore this effect have a greater impact in the axial direction. Phase-only jump  $\delta\varphi$  is a consequence of motion in the axial direction only, and is proportional to the axial displacement  $\delta z$  and the central wavenumber,  $\delta\varphi = 2k_c\delta z$ , where the factor of two is due to the double-pass, reflection geometry. Since  $k$  is typically a relatively large value (of the order of  $10^6$ ) relatively small displacements  $\delta z$  can produce significant phase jumps  $\delta\varphi$ , and this is why phase sensitive techniques can measure very small displacement using optical interferometry, but in the case of CAC this is an undesired phase contribution that in general have a greater influence than complex amplitude shift effect. By this reason, in some cases there is not an evident displacement in the tomogram intensity due to motion, yet there may be phase jumps reducing phase stability.

In practical terms, motion artifacts are negligible within one A-line acquisition under controlled circumstances, in the case of SDOCT because the parallel acquisition in  $k$ -space, and in SSOCT because the high A-line acquisition rate. However, motion artifacts may appear during acquisition of multiple A-lines and more significantly during acquisition of multiple B-scans which have a longer repetition time. Complex amplitude shifts appear as relative displacements between A-lines or B-scans, whereas phase-only jumps produce a relative phase offset between A-lines or B-scans.

Figure 2.13 illustrates the effect of motion artifacts in OCT images and phase stability, using a simulated B-scan generated similarly to that of Fig.2.10, except that axial motion was added when computing the  $n$ -th A-line by changing the position  $z$  of all scatters by  $z+\delta z_n$ , where  $\delta z_n$  represents the magnitude of motion, with random values inside a predefined range for every A-line. This corresponds to a rigid body or *bulk* motion because the entire sample is displaced by the same amount in every A-line. The simulated intensity B-scan with a static sample is shown in Fig.2.13a), displaying defocus away from the focal plane in  $z = 0$ , this image was re-generated inducing inter-A-line motion as plotted in Fig.2.13d), and the resulting intensity B-scan shown in Fig.2.13b) exhibits spurious relative shifts between A-lines, which in this case are evident because the magnitude of motion is of the order of the axial resolution of  $5 \mu\text{m}$ .

To evaluate phase stability, Fig.2.13 shows phase images, denoted as  $\arg\{\cdot\}$ , where a threshold was used to display only regions with high intensity, corresponding to the point scatterers. Fig.2.13e) is the phase with the static sample, exhibiting a stochastic but smooth behavior, distinctive of phase stable images, opposed to the phase image after inducing motion shown in Fig.2.13e) that exhibits very poor

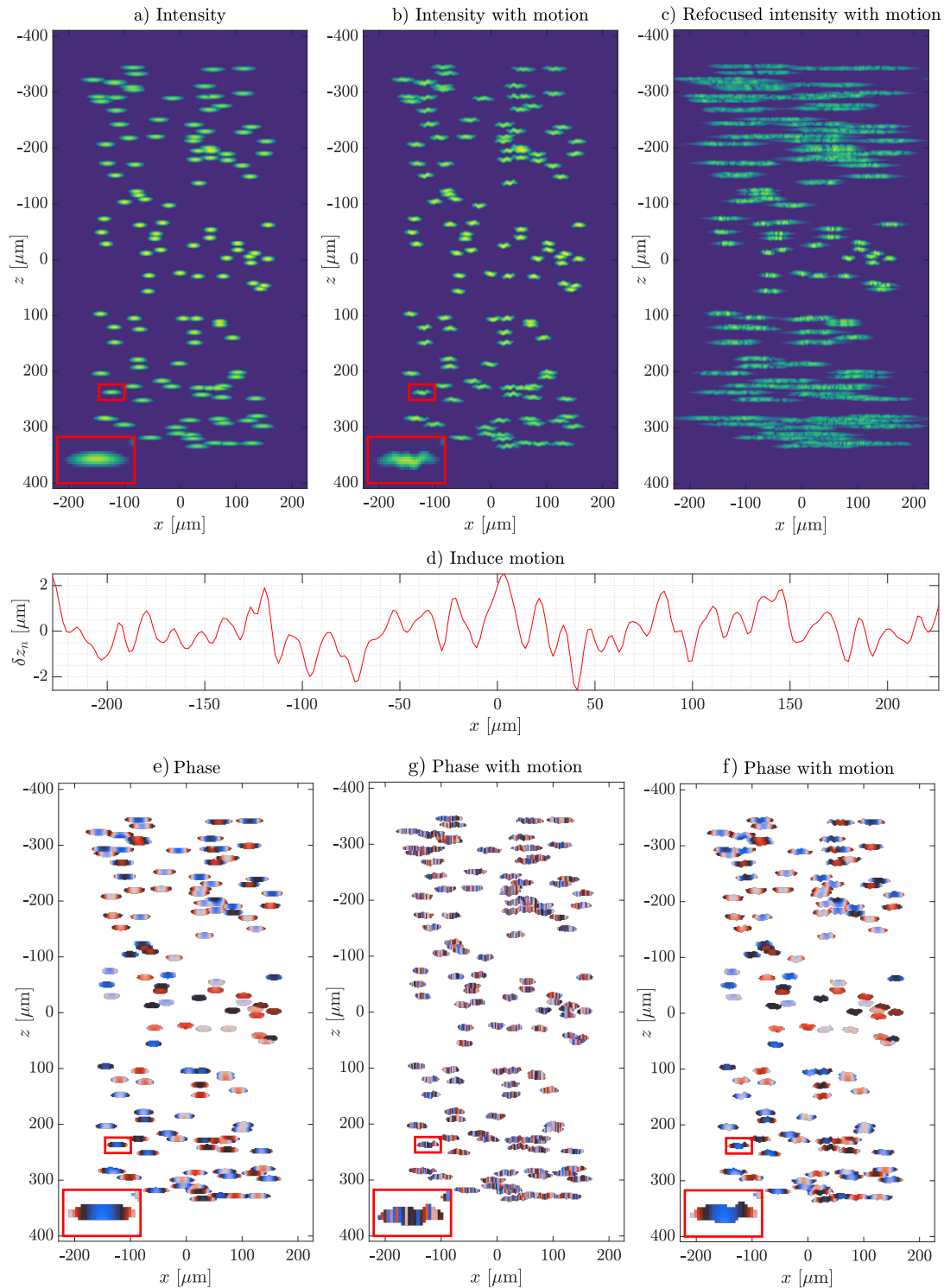


Figure 2.13: Illustration of the impact of motion in digital refocusing. a) OCT image simulated using the forward model, a) with static sample; b) with sample motion shown in d), that results in the unsuccessful digital refocused image c) refocusing. Note the relative shift between A-lines when comparing the insets in red rectangles.

phase stability because of the relative shifts between A-lines, also observable in the

intensity image in Fig.2.13b), and more importantly due to the random phase offsets induced by Doppler jumps, not observable in the intensity image in Fig.2.13b). Lack of phase stability frustrates the operation of digital refocusing or any other phase-dependent aberration correction method, as is evident in Fig.2.13c). To compare the influence of each effect of motion, Fig.2.13f) shows the phase when ignoring the motion-induced phase offsets, thus considering only the complex amplitude shifts, and it can be noted that phase is smoother than that of Fig.2.13g) that include both motion artifacts, however, even ignoring phase jumps, in this example complex amplitude shifts alone are strong enough to frustrate any aberration correction.

To determine that certain tomogram has enough phase stability for a phase-dependent technique to work properly is somewhat not possible, instead, it is possible to recognize when phase stability is not enough for such techniques to provide reliable results. Some systematic studies have been carried out to show the effect of various types of motion on defocus correction, namely, 1-D Brownian motion, steps functions and sinusoidal motion, and this helped to determined thresholds for admissible motion magnitudes for successful aberration correction [?] to assist the design of OCT systems, for instance to determine an adequate imaging speed. Such works include simulated studies, as well as experimental studies with ex vivo sample, and a further extension with in vivo imaging, finding out that in terms of motion-induce phase noise, axial motion plays indeed the most important role in phase stability, although in some experimental scenarios traverse motion may be significant as well.

## Phase stabilization

Given that the presence of phase noise in acquired tomograms is quite difficult to avoid or suppress experimentally, phase stabilization in post-processing have been developed for phase-dependent imaging techniques in OCT like aberration correction and Doppler OCT. Such techniques were designed to correct for phase jumps between A-lines, whether they arise from sample-motion or the system itself, but they cannot address complex amplitude shifts so that they must be small enough to be considered negligible.

An early phase stabilization approach employs a reference signal consisting in an highly reflective flat surface in the sample arm, like a mirror or even a coverslip. The phase of this reference signal is assumed to be space-invariant, any phase jump between A-lines must be due to phase noise. The procedure consist in identifying and extracting the reference signal in the tomogram  $S_R(m, n, l)$ , which should appear across the entire lateral field of view but occupy only a small set of pixels  $L$  in the axial direction, and in a phase stable tomogram it should have a constant phase.

Then, the phase difference between adjacent A-lines are computed as

$$\delta\varphi(m, n) = \sum_{l \in L} S_R^*(m + 1, n, l) S_R(m, n, l), \quad (2.35)$$

where \* denotes complex conjugate and the summation over  $L$  is to perform a phasor average. Phase differences  $\delta\varphi(m, n)$  are relative to consecutive A-lines, the absolute phase differences  $\varphi(m, n)$  with respect to a reference A-line, typically first A-line, are calculated using a cumulative sum as

$$\varphi(m, n) = \sum_{\hat{m}}^m \delta\varphi(\hat{m}, n). \quad (2.36)$$

Finally, the phase-corrected tomogram  $\tilde{S}(m, n, l)$  is corrected applying the conjugate phase differences,

$$\tilde{S}(m, n, l) = S(m, n, l) e^{-i\varphi(m, n)} \quad (2.37)$$

To summarize, this phase stabilization process consist in applying a conjugate phase offset that is determined for each A-line using the phase difference between successive A-lines considering only a region of the signal containing a reference constant phase. There are some important features to remark. First, the correction phase is depth-independent; it consists of a global phase offset for every A-line, so that it cannot correct for phase-jitter which is a depth-dependent ramp phase noise as noted in Eq.(2.9), an extension to cover phase-jitter is possible and has been developed as will be explained later. Second, the need of a reflective surface in the sample arm is difficult to implement in practical terms, specially for *in vivo* imaging where it is not easy to add a mirror in the sample arm directly. A very used approach is to separate the sample arm into two paths, one for the sample and the other for a mirror, but this is based on hardware modifications not present in basic OCT systems setups.

## CHAPTER 3

---

# COMPUTATIONAL ABERRATION CORRECTION IN PHASE UNSTABLE OCT: SHARP

### **3.1. SHARP: A CAO technique for OCT**

- 3.1.1. Phase stability assessment
- 3.1.2. Description of the method

### **3.2. Proof of concept experimental validation**

### **3.3. Extending SHARP**

- 3.3.1. Motion artifacts correction
- 3.3.2. Spatially-varying aberrations correction
- 3.3.3. Complex amplitude noise reduction

## CHAPTER 4

---

# COMPLEX SHOT NOISE REDUCTION IN OCT: CTNode

## CHAPTER 5

---

# EXPERIMENTAL APPLICATION

## CHAPTER 6

---

# CONCLUSIONS AND FUTURE WORKS

Dadas las limitaciones actuales de estabilidad de fase de los sistemas de OCT más comunes, la propuesta para la tesis de maestría consiste en corregir aberraciones en tomogramas sin estabilidad de fase para mejorar la calidad de las imágenes, utilizando técnicas de posprocesamiento y sin emplear configuraciones o modificaciones experimentales en los sistemas, tanto en muestras como

---

## REFERENCES